A&A 468, 379–390 (2007)
DOI: 10.1051/0004-6361:20066320

Astronomy & Astrophysics
Special feature

The XMM-Newton extended survey of the Taurus molecular cloud

The XMM-Newton Optical Monitor survey of the Taurus molecular cloud⋆,⋆⋆

M. Audard[1,⋆⋆⋆], K. R. Briggs[2], N. Grosso[3], M. Güdel[2], L. Scelsi[4], J. Bouvier[3], and A. Telleschi[2]

[1] Columbia Astrophysics Laboratory, Columbia University, 550 West 120th Street, Mail code 5247, New York, NY 10027, USA
e-mail: audard@astro.columbia.edu
[2] Paul Scherrer Institut, Würenlingen and Villigen, 5232 Villigen PSI, Switzerland
e-mail: [briggs;guedel;atellesc]@astro.phys.ethz.ch
[3] Laboratoire d'Astrophysique de Grenoble, Université Joseph Fourier, 38041 Grenoble Cedex 9, France
e-mail: [Nicolas.Grosso;Jerome.Bouvier]@obs.ujf-grenoble.fr
[4] Dipartimento di Scienze Fisiche ed Astronomiche, Università di Palermo, Piazza del Parlamento 1, 90134 Palermo, Italy
e-mail: scelsi@astropa.unipa.it

Received 30 August 2006 / Accepted 8 November 2006

ABSTRACT

Context. The Optical Monitor (OM) on-board *XMM-Newton* obtained optical/ultraviolet data for the *XMM-Newton* Extended Survey of the Taurus Molecular Cloud (XEST), simultaneously with the X-ray detectors.
Aims. With the XEST OM data, we study the optical and ultraviolet properties of TMC members, and to perform correlative studies between the X-ray and OM light curves. In particular, we aim to determine whether accretion plays a significant role in the optical/ultraviolet and X-ray emissions. The Neupert effect in stellar flares is also investigated.
Methods. Coordinates, average count rates and magnitudes were extracted from OM images, together with light curves with low time resolution (a few kiloseconds). For a few sources, OM FAST mode data were also available, and we extracted OM light curves with high time resolution. The OM data were correlated with Two Micron All Sky Survey (2MASS) data and with the XEST catalogue in the X-rays.
Results. The XEST OM catalogue contains 2148 entries of which 1893 have 2MASS counterparts. However, only 98 entries have X-ray counterparts, of which 51 are known TMC members and 12 additional are TMC candidates. The OM data indicate that accreting stars are statistically brighter in the U band than non-accreting stars after correction for extinction, and have U-band excesses, most likely due to accretion. The OM emission of accreting stars is variable, probably due to accretion spots, but it does not correlate with the X-ray light curve, suggesting that accretion does not contribute significantly to the X-ray emission of most accreting stars. In some cases, flares were detected in both X-ray and OM light curves and followed a Neupert effect pattern, in which the optical/ultraviolet emission precedes the X-ray emission of a flare, whereas the X-ray flux is proportional to the integral of the optical flux.

Key words. stars: coronae – stars: flare – stars: formation – stars: pre-main sequence – surveys – X-rays: stars

1. Introduction

The *XMM-Newton* Extended Survey of the Taurus Molecular Cloud (XEST) (Güdel et al. 2007a) is primarily focused on the X-ray emission of young stellar and substellar objects (YSOs). However, since *XMM-Newton* (Jansen et al. 2001) is capable of observing simultaneously in the X-rays with the European Photon Imaging Cameras (Strüder et al. 2001; Turner et al. 2001) and the Reflection Grating Spectrometers (den Herder et al. 2001), and in the optical and ultraviolet regimes with the Optical Monitor (Mason et al. 2001), we have obtained deep images and sensitive light curves, primarily in the U band, but also in the near-ultraviolet regime in some cases.

Simultaneous X-ray and optical/UV coverage of young stars provides the ideal means to study the physical processes occurring in the stellar upper atmospheres (e.g., Stelzer et al. 2003) or the interactions between an accretion disk and a star. For example, our understanding of the physics of flares in magnetically active stars can benefit from simultaneous monitoring. In the chromospheric evaporation model (e.g., Antonucci et al. 1984), magnetic reconnection in the corona injects accelerated particles propagating along the magnetic field lines, heating the chromosphere and the transition region through collisions (evident in emission in the optical/ultraviolet). Heated material (visible in soft X-rays) then moves up along the magnetic field lines into the corona where it cools. A "Neupert" effect (Neupert 1968) should, therefore, be observed in the optical/UV and X-ray light curves, in which the time profile of the X-ray light curve is proportional to the time integral of the optical light curve (conversely, the optical flux has the same time profile as the derivative of the X-ray flux). This effect has been observed in

⋆ Appendix B is only available in electronic form at http://www.aanda.org
⋆⋆ Appendix A is only available in electronic form at the CDS via anonymous ftp to cdsarc.u-strasbg.fr (130.79.128.5) or via http://cdsweb.u-strasbg.fr/cgi-bin/qcat?J/A+A/468/379
⋆⋆⋆ *New address (since September 2006):* Integral Science Data Centre, Ch. d'Ecogia 16, 1290 Versoix, Switzerland & Geneva Observatory, University of Geneva, Ch. des Maillettes 51, 1290 Sauverny, Switzerland; e-mail: Marc.Audard@obs.unige.ch

main-sequence active stars (Hawley et al. 1995; Güdel et al. 2002a; Hawley et al. 2003; Güdel et al. 2004; Mitra-Kraev et al. 2005). Stellar Neupert effects were also reported from X-rays and radio gyrosynchrotron emission of accelerated particles gyrating along the magnetic fields (Güdel et al. 1996; Güdel et al. 2002b; Smith et al. 2005), although not all multi-wavelength observations necessarily detect typical Neupert effects (e.g., Stelzer et al. 2003; Osten et al. 2005), probably because of different conditions in the flaring source.

Optical studies of young stars have also provided evidence of rotational modulation of active regions, suggesting that a solar-type magnetic activity operates in T Tauri stars (e.g., Rydgren & Vrba 1983; Rydgren et al. 1984; Bouvier et al. 1988; Bouvier & Bertout 1989; Bouvier 1990; Bouvier et al. 1993; Vrba et al. 1993; Bouvier et al. 1995, 1997, etc.). Detailed analyses indicate that weak-line T Tauri stars (WTTS) on average rotate faster than the still accreting classical T Tau stars (CTTS), possibly due to disk locking or loss of angular momentum due to stellar winds in CTTS (Bouvier et al. 1993). In addition, rotational modulation in some CTTS can be dominated by hot spots due to accreting material falling from the accretion disk onto the stellar surface (Vrba et al. 1986; Bouvier & Bertout 1989; Vrba et al. 1989; Bouvier et al. 1993; Herbst et al. 1994; Bouvier et al. 1995).

Although most low-mass accreting stars display X-ray spectra typical of hot coronal plasma, at least a few of them display either lower temperature spectra or densities atypical of a stellar corona, or both, indicating that accretion could play a significant role in the production of X-rays (Kastner et al. 2002; Stelzer & Schmitt 2004; Schmitt et al. 2005; Ness & Schmitt 2005; Robrade & Schmitt 2006; Telleschi et al. 2007a). In some cases, the soft X-ray component could arise from shocks in jets originating from the young accreting stars (Güdel et al. 2005; Kastner et al. 2005; Güdel et al. 2007b). In low-mass young stars with optical outbursts, the sudden rise in mass accretion rate also appears to impact on the X-ray emission. During the accretion outburst of V1647 Ori, the mean X-ray flux closely tracked the near-infrared luminosity, and the X-ray spectrum hardened (Kastner et al. 2004; Grosso et al. 2005; Kastner et al. 2006). On the other hand, Audard et al. (2005) observed little X-ray flux variability in the early epochs of the outburst, in contrast to the optical/near-infrared flux enhancements, but they found a change in the X-ray spectrum of the young star V1118 Ori from a dominant hot plasma pre-outburst to a cool plasma during the outburst. The coronal hot plasma essentially disappeared, probably because the inner accretion disk disrupted the coronal loops. Finally, accretion may also be a dominant mechanism in the more massive, accreting Herbig Ae stars (Swartz et al. 2005), although magnetically confined winds may be a good alternative as well (Telleschi et al. 2007b).

Optical and X-ray correlations of young stars can, therefore, provide important information on flare physics and rotational modulation due to spots and active regions in magnetically active stars (e.g., Flaccomio et al. 2005) or due to hot accretion spots. Multi-wavelength studies are ideal to determine to what extent accretion plays a significant role in the production of X-rays in young accreting stars. Recently, Stassun et al. (2006) studied the correlation between the optical (*BVRI*) and X-ray light curves of young stars in the Orion Nebula Cluster. The optical observations covered the 13-day *Chandra* observation of the cluster, and the typical exposure times ranged from 5 s for short exposures to 420–720 s for long exposures. However, the observing cadence was about 1 per hour for each filter. Stassun et al. (2006) found little evidence of correlations between the optical and X-ray variability, although there were some exceptions.

In this paper, we report on the Optical Monitor (OM) data obtained as part of the XEST. Section 2 describes the OM data, whereas we introduce the OM catalogue in Sect. 3. The vast majority of our optical (and UV in a few cases) detections is of sources which are probably foreground or background sources. We provide the full OM catalogue of detected sources as online material, although this paper focuses specifically on known or probable TMC members (including new membership candidates identified by Scelsi et al. 2007). A separate paper focuses on the OM survey of brown dwarfs (Grosso et al. 2007a). Section 4 makes use of the OM data and data compiled by Güdel et al. (2007a) in order to derive basic properties of the OM TMC sample. Since the OM and X-ray detectors observed simultaneously, we also study correlations between the optical/ultraviolet and X-ray light curves for TMC members in Sect. 5.

2. Optical Monitor data

The Optical Monitor (OM; Mason et al. 2001) is a 30-cm optical/UV telescope that can provide coverage in the optical and UV regimes (bandwidth 180–600 nm) simultaneously with the X-ray cameras. The OM detector is a micro-channel plate (MCP) intensified CCD. The final array has a format of 2048×2048 pixels, each pixel having a size of about 0.″48, leading to a square field-of-view (FOV) of about 17′ × 17′, which covers the central part of the X-ray cameras (15′-radius FOV). The OM carries a wheel of filters (*V*, *U*, *B*, *UVW1*, *UVM2*, *UVW2*, and a broad white light filter) and 2 grisms for the visible and UV ranges. In this paper, we report on OM data taken with the *U* (≈300–400 nm) and *UVW2* (≈175–250 nm) filters. The OM point-spread-function varies from 1.″4 to 2″, depending on the filter. The OM can operate in the "Imaging" or "Fast" modes; of particular interest here, in the default Imaging mode ("Image" in Table 1), a set of 5 *consecutive* exposures is taken, each covering a different portion of the FOV. In each of the 5 exposures, a large window ($W_{1,\ldots,5}$; with 1″ pixels) is complemented by a smaller central imaging mode window of size 2′ × 2′ with 0.″5 pixel resolution (W_0). Thus, the sequence is exposure 1: W_0+W_1, exposure 2: W_0+W_2, etc. until exposure 5: W_0+W_5, after which the sequence can start again. An example of the configuration can be found in the *XMM-Newton* Users' Handbook (Ehle et al. 2005). In the default Fast mode ("Image Fast" in Table 1), a similar set of images is obtained together with an additional central window (CW; 22 × 23 pixels, i.e., 10.″5 × 10.″5) that is operated in fast mode with a time resolution of 0.5 s. Consequently, the sequence of images is exposure 1: W_0+W_1+CW, exposure 2: W_0+W_2+CW, etc. until exposure 5: W_0+W_5+CW. This means that the on-axis target should be monitored continuously with high time resolution, and 5 times in the small central 2′ × 2′ W_0 imaging window (with each an exposure equal to the integration time of the exposure), and once in the large, central 1″-pixel window. If a secondary target is located in a sky area covered by the small central imaging window W_0, it is observed in a similar fashion as above, except that no fast mode data is available. If it is located in an area outside the 2′ × 2′ window, it will be observed only in one of the 5 consecutive large imaging window, i.e., once per OM exposure. Clearly, the best time coverage for a secondary target is when it is located in a sky area covered by the small central window. Note that other imaging modes can be used as well. For example, in "Full-Frame" imaging mode, images of the whole OM FOV can be obtained either in full resolution (0.″5 pixel size; "High Resolution") or in low (1″ pixel size; "Low Resolution"). Additional user-specified mode can be used as well (see XEST-28 in Table 1). Because the OM FOV

Table 1. OM-specific observation Log.

XEST	ObsID	RA[a]	δ[a]	PA[a]	OM	OM	Fast	Image
		h m s	° ′ ″	(°)	Filter	Mode	Data	Exposures
01	0301500101	04 21 59.4	+19 32 06	80.01	*UVW1*	Image Fast	Y	18×3540 s
02	0203540201	04 27 19.6	+26 09 25	82.05	*U*	Full-Frame Low Res[b]	N	4×5000 s, 3170 s
03	0203540301	04 32 18.9	+24 22 28	81.92	*U*	Image Fast	Y	20×1500 s
04	0203540401	04 33 34.4	+24 21 08	261.88	*U*	Image Fast	Y	12×1640 s
05	0203540501	04 39 34.9	+25 41 46	262.68	*U*	Full-Frame Low Res[b]	N	4000 s, 4479 s, 2×5000 s
06	0203540601	04 04 42.9	+26 18 56	79.03	*U*	Full-Frame Low Res[b]	N	4×5000 s
07	0203540701	04 41 12.5	+25 46 37	262.61	*U*	Full-Frame Low Res[b]	N	3×5000 s, 1679 s
08	0203540801	04 35 52.9	+22 54 23	81.90	*U*	Image Fast	Y	10×1260 s, 10×1240 s
09	0203540901	04 35 55.1	+22 39 24	261.85	*U*	Full-Frame Low Res[b]	N	5×5000 s
10	0203542201	04 42 20.9	+25 20 35	262.27	*U*	Image Fast	Y	15×1780 s
11	0203541101	04 21 51.1	+26 57 33	81.69	*U*	Full-Frame Low Res[b]	N	5×5000 s
12	0203542101	04 35 17.4	+24 15 00	261.59	*U*	Image Fast	Y	15×1500 s
13	0203541301	04 29 52.0	+24 36 47	81.55	*U*	Full-Frame Low Res[b]	N	3×5000 s, 1679 s
14	0203541401	04 30 30.6	+26 02 14	262.72	*U*	Full-Frame Low Res[b]	N	2×5000 s, 4179 s
15	0203541501	04 29 42.4	+26 32 51	262.81	*U*	Full-Frame Low Res[b]	Y	12×1260 s, 5×1380 s
16	0203541601	04 19 43.0	+27 13 34	–	–	–	–	–
17	0203541701	04 33 21.2	+22 52 41	261.86	*U*	Full-Frame Low Res[b]	N	3×4170 s
18	0203541801	04 33 54.7	+26 13 28	83.07	*U*	Image Fast	Y	5×1360 s, 5×1260 s, 10×1200 s
19	0203541901	04 32 43.0	+25 52 32	82.83	*U*	Image Fast	Y	15×1680 s, 5×1660 s
20	0203542001	04 14 12.9	+28 12 12	78.06	*U*	Image Fast	Y	10×2480 s
21	0101440701	04 21 59.0	+28 18 08	–	–	–	–	–
22	0109060301	04 31 39.0	+18 10 00	83.58	*UVW2*	Image[c]	N	5×1000 s
23	0086360301	04 18 31.2	+28 27 16	259.74	*UVW2*	Image	N	5×1000 s
24	0086360401	04 18 31.2	+28 27 16	259.67	*UVW2*	Image	N	5×1000 s
25	0152680201[d]	04 34 55.5	+24 28 54	244.71	*UVW2*	Image	N	10×980 s
26	0101440801	04 55 59.0	+30 34 02	–	–	–	–	–
27	0201550201	03 54 07.9	+31 53 01	–	–	–	–	–
28	0200370101	04 19 15.8	+29 06 27	82.13	*UVW1*	Science User Defined[c,e]	Y	25×4000 s, 2×2200 s

[a] Nominal boresight coordinates (J2000.0) and average spacecraft position angle. [b] 1024×1024 pixel images with 1″ pixel size ($17' \times 17'$). [c] Grism exposures taken after the imaging exposures. [d] This observation is part of a campaign on AA Tau that will be presented extensively elsewhere. [e] 624×624 pixel images with 0.″5 pixel size ($5' \times 5'$) together with a $10.''5 \times 10.''5$ window in Fast mode.

is smaller ($17' \times 17'$) than the EPIC field-of-view (15′ radius), several interesting X-ray sources did not fall on the OM detector, and, therefore, no photometry or light curve could be obtained.

The OM data were reduced with the *XMM-Newton* Science Analysis System (SAS) 6.1. We have processed the "Imaging" and "Fast" mode data using the metatasks *omichain* and *omfchain*, respectively, with default parameters, except for the *omdetectminsignificance* parameter of *omichain*, which determines the minimum significance of a source to be included in the source-list file and which we changed from 1.0 to 3.0. In Table 1, we provide an observation log of the XEST fields (Güdel et al. 2007a), with an emphasis on the OM-specific parameters. In particular, we provide the imaging mode and emphasize when a Fast mode window was available, and we provide the exposures of the individual imaging windows. For example, for XEST-01, for the first exposure, the imaging windows W_0 and W_1 observed simultaneously for 3540 s, then (after some overhead delay), W_0 and W_2 observed for another 3540 s, etc. Since the XEST-01 OM data were obtained in FAST mode as well, the CW window was operating in parallel. For XEST-02, $W_0 + W_1$, $W_0 + W_2$, $W_0 + W_3$, $W_0 + W_4$ each observed for 5000 S, while the last exposure with windows W_0 and W_5 observed for 3170 s only.

For "Imaging" mode data, we obtained images and source lists for individual exposures, a mosaicked image, and a merged source list. Each individual source list included, in particular, the exposure source number, sky and galactic coordinates, raw and corrected count rates, magnitudes, quality flags, and the source identification in the final source list. Consequently, it was possible, knowing the source identification, to obtain exposure-specific count rates and magnitudes, i.e., low time-resolution light curves[1]. However, SAS 6.1 identified a significant number of spurious sources, mostly in the ghost image near a bright star produced by internal reflection of light within the detector window, in the enhanced "ring" of emission near the center of the detector (due to the reflection of diffuse sky light from outside the FOV), and in fixed pattern noise around bright sources (Ehle et al. 2005). We manually inspected the mosaicked image, merged source list identifications, and removed obvious misidentifications. We also modified the merged source list to ensure that the same source had the same source identification in each exposure; indeed, the *omsrclistcomb* task did not combine the source lists accurately in a few cases, i.e., mostly bright sources for which strong fixed pattern noise introduced small positional inaccuracies that were not properly identified by SAS 6.1. We note that SAS 6.5 eliminates most of the above issues; however, this version of the SAS incorrectly combines the source lists, and, therefore, we preferred not to use it. Figure 1 shows an example of an OM image with some artefacts.

For "Fast" mode data, in addition to individual images, we obtain event lists and time series files with high time resolution (the default value is 10 s with *omfchain*) for each exposure. We merged the different time series files into a single time series file for further analysis.

[1] For point sources identified in both the small $0.''5 \times 0.''5$ and the larger $1'' \times 1''$ central windows, we used count rates and magnitudes from the small window because of the smaller pixel bin size and of the more frequent time sampling.

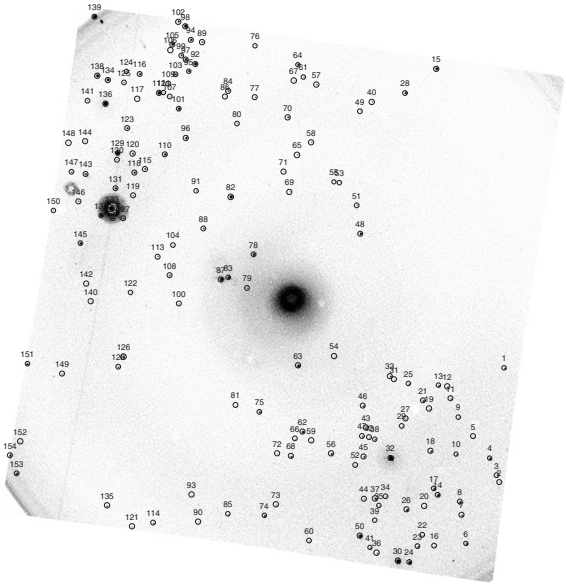

Fig. 1. Example of an OM image. This rich field (XEST-11, toward FS Tau) shows artefacts, such as the "ring" of emission at the center (due to the reflection of diffuse sky light from outside the FOV), fixed pattern noise around the bright source XEST-11-OM-133 (HD 283579, which is not classified as a TMC member), and a ghost ring below source XEST-11-OM-147 which is also caused by XEST-11-OM-133. Other artefacts can be seen (trail along the bright source, defects on the detector).

Table 2. OM astrometric correction vectors in arcseconds.

XEST	ΔX	ΔY	rms
01	3.086	−2.462	0.90
02	4.338	−1.016	0.62
03	3.320	−0.970	0.52
04	−1.471	3.632	0.83
05	−3.561	4.579	0.52
06	3.948	−3.227	0.57
07	−3.240	4.412	0.99
08	2.955	−0.800	0.81
09	−2.728	5.588	0.62
10	−2.219	2.623	0.61
11	3.847	−0.137	0.61
12	−2.675	3.093	0.61
13	2.143	−1.162	0.86
14	−4.529	3.239	0.68
15	−3.891	5.163	0.71
17	−3.824	5.114	0.58
18	2.893	−1.391	0.92
19	3.617	−0.044	0.62
20	6.201	−5.232	0.48
22	1.586	−1.008	0.06
23	0.368	1.105	0.00[a]
24	−1.363	0.720	0.00[a]
25	−3.065	4.090	1.63
28	5.519	−0.994	0.77

[a] Only V410 Tau detected in the OM.

3. Optical Monitor catalogue

A catalogue of OM sources was compiled, cross-checked with the Two Micron All Sky Survey (2MASS) and the XEST X-ray sources. We provide average photometry and source coordinates as compiled in the combined source lists in the imaging mode data. We calculated boresight corrections to OM coordinates by cross-correlating with the 2MASS catalogue (search radius of 3″) and by means of iterative steps until the median position offsets became zero. Table 2 provides the position offsets ($\Delta X, \Delta Y$) in arcseconds ($\mathrm{RA_{corr}} = \mathrm{RA_{OM}} + \Delta X/\cos(\delta_{\mathrm{2MASS}})$ and $\delta_{\mathrm{corr}} = \delta_{\mathrm{OM}} + \Delta Y$). We also cross-correlated the OM and the X-ray catalogues (Güdel et al. 2007a) using 2MASS-corrected coordinates (search radius of 3″). Minor manual interventions were necessary when two close sources were separated in the OM but not in X-rays (UZ Tau E+W(AB), HP Tau/G2 and HP Tau/G3 AB). We used the same detection parameters for all observations. Consequently, the source detection process is not optimized for each exposure; however, a visual inspection showed that the chosen parameters were generally sufficient, although we do not claim completeness in the XEST OM catalogue.

Table 3 provides the first 30 entries of the full OM catalogue, in increasing right ascension. In Col. 1, we provide the catalogue source number. Columns 2–4 provide the 2MASS-corrected OM right ascension and declination and the positional error Δ (including the rms error on the boresight shift, which was added in quadrature to the statistical 1-sigma positional error calculated for each source). Column 5 provides the XEST OM identification in the xx-OM-zzz notation in Col. 2, where xx refers to the XEST exposure and zzz refers to the OM identification for this XEST exposure. Columns 6 and 7 give the 2MASS cross-identification, if found, and the offset ρ_1 between the OM corrected coordinates and the 2MASS coordinates. Columns 8 and 9 give the XEST X-ray identification (in xx-yyy notation, see Güdel et al. 2007a), if found, and the offset ρ_2 between the OM and X-ray corrected coordinates. Column 10 gives the average magnitude and its uncertainty, and Col. 11 the detection significance. For clarity, we have added in the exponent a ‡ character if the filter was *UVW2* and a † character if the filter was *UVW1*. No special character was added for the commonly used *U* filter. We provide the full OM catalogue as online material at the CDS (Table A.1).

The XEST OM catalogue contains 2148 entries, among which 1893 have 2MASS counterparts and 98 have XEST X-ray counterparts. Out of these 98 sources, 51 are TMC members according to the master list from Güdel et al. (2007a) and 12 are new TMC candidates identified by Scelsi et al. (2007). Thus 35 OM sources had X-ray counterparts but were not classified as TMC members or candidates. Note that V410 Tau ABC (XEST-23-032 & XEST-24-028) was counted twice in the OM catalogue since it was observed in two different XEST observations. In addition, UZ Tau E+W(AB) (XEST-19-049) were not separated in X-rays but were so in the OM (UZ Tau W = XEST-19-OM-092, UZ Tau E = XEST-19-OM-094). Similarly, the X-ray source XEST-08-051 was attributed to both HP Tau/G3 AB and HP Tau/G2 (centroid fitting suggests that the X-rays come mostly from HP Tau/G2); however, they were separated in the OM data (XEST-08-OM-038 for HP Tau/G3 AB and XEST-08-OM-040 for HP Tau/G2).

There were 2 TMC members detected in the OM but not detected in X-rays with *XMM-Newton* (FV Tau/c AB, XEST-02-OM-020 and 2MASS J04141188+2811535, XEST-20-OM-002). However, FV Tau/c AB is very close to FV Tau AB (XEST-02-013 = XEST-02-OM-017) and its faint X-ray emission may have been overshadowed by the stronger X-ray flux of FV Tau AB. Note that FV Tau/c AB was detected by *Chandra* (Güdel et al. 2007a). A similar case occurred for the brown dwarf 2MASS J04141188+2811535 (Luhman 2004), which is close to the X-ray bright V773 Tau (XEST-20-042 = XEST-20-OM-003). The OM data of the brown dwarf is addressed in a separate paper (Grosso et al. 2007a).

While the above detection numbers start from OM detections, we have also taken a different approach, starting from the

Table 3. XEST OM catalogue (first thirty entries).

#	RA_{corr} h m s	δ_{corr} ° ′ ″	Δ (″)	XEST OM	2MASS	ρ_1 (″)	XEST	ρ_2 (″)	Mag[a]	Signif.
1	04 03 59.95	+26 23 31.8	0.60	06-OM-001	04035989+2623319	0.73			20.62 ± 0.09	15.2
2	04 04 00.62	+26 24 43.9	0.60	06-OM-002	04040056+2624441	0.81			19.05 ± 0.04	21.4
3	04 04 00.78	+26 23 29.8	0.57	06-OM-003	04040075+2623295	0.45			16.79 ± 0.01	114.3
4	04 04 02.24	+26 24 59.7	0.57	06-OM-004	04040217+2624595	0.84			16.02 ± 0.00	176.6
5	04 04 03.27	+26 22 24.6	0.63	06-OM-005	04040327+2622244	0.13			19.95 ± 0.09	10.4
6	04 04 03.59	+26 25 02.8	0.60	06-OM-006					18.33 ± 0.03	38.5
7	04 04 04.69	+26 24 48.7	0.63	06-OM-007	04040467+2624478	0.84			20.15 ± 0.10	8.5
8	04 04 07.46	+26 19 10.4	0.61	06-OM-008	04040741+2619102	0.60			19.19 ± 0.04	19.6
9	04 04 08.17	+26 17 50.7	0.59	06-OM-009	04040814+2617508	0.33			18.38 ± 0.01	37.5
10	04 04 08.31	+26 19 18.6	0.63	06-OM-010					20.46 ± 0.17	6.2
11	04 04 08.43	+26 19 49.0	0.63	06-OM-011					20.15 ± 0.12	8.4
12	04 04 09.26	+26 19 10.1	0.61	06-OM-012	04040919+2619098	0.88			19.26 ± 0.12	18.1
13	04 04 09.35	+26 14 06.2	0.59	06-OM-013	04040936+2614059	0.32			18.65 ± 0.03	29.7
14	04 04 09.50	+26 15 16.7	0.64	06-OM-014					20.87 ± 0.08	4.4
15	04 04 09.57	+26 22 03.8	0.58	06-OM-015	04040952+2622034	0.62			17.38 ± 0.02	78.6
16	04 04 09.87	+26 19 00.6	0.64	06-OM-016					20.51 ± 0.16	6.0
17	04 04 10.24	+26 21 58.7	0.60	06-OM-017	04041018+2621581	0.98			18.94 ± 0.05	24.4
18	04 04 10.44	+26 22 57.3	0.64	06-OM-018					20.84 ± 0.14	4.7
19	04 04 10.53	+26 19 01.3	0.58	06-OM-019	04041051+2619011	0.33			17.67 ± 0.03	63.8
20	04 04 11.02	+26 10 57.7	0.61	06-OM-020	04041104+2610573	0.51			19.19 ± 0.06	19.6
21	04 04 11.19	+26 20 04.0	0.61	06-OM-021	04041116+2620036	0.50			19.57 ± 0.05	14.3
22	04 04 11.22	+26 10 47.7	0.63	06-OM-022					20.21 ± 0.19	7.7
23	04 04 11.34	+26 25 16.4	0.57	06-OM-023	04041129+2625162	0.65			16.77 ± 0.01	115.6
24	04 04 11.82	+26 11 41.1	0.64	06-OM-024					20.92 ± 0.17	4.1
25	04 04 11.83	+26 25 03.8	0.62	06-OM-025	04041178+2625035	0.64			19.62 ± 0.13	13.3
26	04 04 11.85	+26 12 03.2	0.62	06-OM-026					19.63 ± 0.09	13.5
27	04 04 11.89	+26 11 24.4	0.59	06-OM-027	04041191+2611239	0.58			18.59 ± 0.04	32.1
28	04 04 11.93	+26 19 12.0	0.60	06-OM-028	04041190+2619118	0.25			19.00 ± 0.05	22.8
29	04 04 12.66	+26 12 44.4	0.63	06-OM-029			06-029	2.86	20.13 ± 0.12	8.7
30	04 04 13.03	+26 11 41.6	0.58	06-OM-030	04041305+2611414	0.27			18.00 ± 0.02	50.3

[a] *U*-band except if identified with † (*UVW1*) or ‡ (*UVW2*).

Table 4. Detection statistics.

	#	Type[a]						
		0	1	2	3	4	5	9
Detected OM sources	2148							
X-ray sources in OM FOV	916							
OM detections not detected in X-rays	2	0	0	1	0	1	0	0
OM detections also detected in X-rays	98							
TMC members detected in X-rays and OM	51	0	1	33	17	0	0	0
TMC candidates detected in X-rays and OM	12							
TMC members detected in X-rays but not in OM	34	0	7	8	8	4	0	7
TMC candidates detected in X-rays but not in OM	21							
TMC members detected in X-rays but outside OM FOV[b]	55	0	1	16	32	4	2	0

[a] See Güdel et al. (2007a) and text for the definition of the object type. [b] Statistics for XEST observations with OM data.

catalog of X-ray sources detected with XEST: we have determined that 916 X-ray sources had coordinates such that they fell on the OM detector. Out of those, only 98 are detected in the OM (see above), while 34 TMC members of TMC detected in X-rays remained undetected in the OM. In addition, 21 new TMC candidates detected in X-rays (Scelsi et al. 2007) were not detected in the OM. Table 4 summarizes the detection statistics pertaining to the OM/X-ray correlations. The object type (as defined by Güdel et al. 2007a, i.e., "0" and "1" for a protostar of Class 0 or Class I, "2" for an accreting (classical) T Tau star usually showing a Class-II IR spectrum, "3" for a weak-lined or Class-III object, "4" for a brown dwarf, "5" for an Herbig Ae star, and "9" for uncertain classifications or other object types) is given when relevant.

No Type 0 object was in our sample since the sole object surveyed was observed by *Chandra* only and remained undetected in X-rays (L1527 IRS; Güdel et al. 2007a). For TMC members detected in the X-rays and falling on the OM FOVs, the OM detection rate was 12.5% (1 out of 8) for Type 1 objects, whereas this rate reached 80.5% in type 2 objects. Type 3 objects had a high 68% detection rate. Interestingly, only 1 brown dwarf was detected in the OM, whereas 11 such objects fell on the OM FOV and 4 of them were detected in X-rays (Grosso et al. 2007a,b). We remind that the numbers reported in Table 4 makes no attempt not to count duplicates. For example, CFHT-Tau 5, detected in X-rays in two XEST observations (XEST-03-031 = XEST-04-003), was counted once in "TMC X-ray OM non-detections" since it fell on the OM detector but remained

Table 5. XEST OM catalogue of TMC members detected in X-rays and in the OM.

RA_{corr}	δ_{corr}	XEST OM	XEST	Name	Type	Mag[a]	$Rate_{OM}$	L_X^b	$Rate_X$
04 14 12.92	+28 12 12.6	20-OM-003	20-042	V773 Tau ABC	3	13.16 ± 0.02	109.13	9.49	1.2113
04 14 13.58	+28 12 49.4	20-OM-004	20-043	FM Tau	2	14.44 ± 0.07	33.76	0.53	0.0611
04 14 17.02	+28 10 57.9	20-OM-005	20-046	CW Tau	2	15.50 ± 0.10	12.73	2.84	0.0015
04 14 17.66	+28 06 09.8	20-OM-006	20-047	CIDA 1	2	18.04 ± 0.15	1.23	0.03	0.0031
04 18 31.10	+28 27 16.2	23-OM-001	23-032	V410 Tau ABC	3	15.85 ± 0.15‡	0.38	3.76	1.2910
04 18 31.10	+28 27 16.2	24-OM-001	24-028	V410 Tau ABC	3	15.69 ± 0.11‡	0.44	4.66	0.8534
04 19 15.84	+29 06 26.7	28-OM-014	28-100	BP Tau	2	13.01 ± 0.10†	46.80	1.37	0.2343
04 21 43.27	+19 34 12.9	01-OM-022	01-028	IRAS 04187+1927	2	19.91 ± 0.31†	0.08	0.91	0.0481
04 21 59.45	+19 32 06.4	01-OM-039	01-045	T Tau N(+Sab)	2	12.00 ± 0.04†	119.13	8.05	0.8189
04 22 02.17	+26 57 31.5	11-OM-087	11-057	FS Tau AC	2	17.57 ± 0.00	1.88	3.22	0.1449
04 22 04.86	+19 34 48.3	01-OM-042	01-054	RX J0422.1+1934	3	19.58 ± 0.08†	0.11	3.11	0.3390
04 22 16.76	+26 54 56.6	11-OM-126	11-079	CFHT-Tau 21	2	18.78 ± 0.18	0.62	0.15	0.0070
04 26 53.56	+26 06 54.6	02-OM-017	02-013	FV Tau AB	2	19.58 ± 0.09	0.30	0.53	0.0212
04 27 04.69	+26 06 15.9	02-OM-028	02-022	DG Tau A	2	13.57 ± 0.05	75.08	0.47[c]	0.0290
04 29 20.73	+26 33 40.3	15-OM-035	15-020	JH 507	3	17.35 ± 0.04	2.30	0.46	0.0382
04 29 23.71	+24 33 00.2	13-OM-001	13-004	GV Tau AB	1	19.20 ± 0.06	0.42	0.95[c]	0.0293
04 29 41.59	+26 32 58.0	15-OM-112	15-040	DH Tau AB	2	14.79 ± 0.04	24.38	8.46	1.0729
04 29 42.52	+26 32 49.1	15-OM-118	15-042	DI Tau AB	3	15.99 ± 0.01	8.11	1.57	0.0979
04 30 44.25	+26 01 24.4	14-OM-258	14-057	DK Tau AB	2	14.09 ± 0.14	46.54	0.92	0.0989
04 31 40.07	+18 13 57.2	22-OM-002	22-047	XZ Tau AB	2	16.70 ± 0.15‡	0.17	0.96	0.2440
04 31 50.61	+24 24 17.7	03-OM-001	03-005	HK Tau AB	2	16.81 ± 0.09	3.81	0.08	0.0045
04 32 15.39	+24 28 59.3	03-OM-007	03-016	Haro 6-13	2	19.22 ± 0.19	0.41	0.80	0.0141
04 32 18.84	+24 22 27.5	03-OM-008	03-019	V928 Tau AB	3	17.65 ± 0.04	1.76	1.05	0.0732
04 32 30.58	+24 19 57.4	03-OM-015	03-022	FY Tau	2	17.83 ± 0.17	1.48	0.81	0.0822
04 32 31.77	+24 20 02.9	03-OM-016	03-023	FZ Tau	2	16.15 ± 0.06	6.99	0.64	0.0232
04 32 42.84	+25 52 31.3	19-OM-092	19-049	UZ Tau W	2	14.23 ± 0.04	40.86	0.89	0.0465
04 32 43.05	+25 52 31.1	19-OM-094	19-049	UZ Tau E	2	14.33 ± 0.02	37.37	0.89	0.0465
04 32 49.10	+22 53 03.0	17-OM-001	17-009	JH 112	2	18.81 ± 0.05	0.60	0.82	0.0357
04 33 34.05	+24 21 16.9	04-OM-018	04-034	GI Tau	2	14.34 ± 0.07	36.97	0.83	0.0364
04 33 34.54	+24 21 05.6	04-OM-020	04-035	GK Tau AB	2	15.50 ± 0.09	12.73	1.47	0.1404
04 33 36.80	+26 09 49.6	18-OM-002	18-019	IS Tau AB	2	18.52 ± 0.11	0.79	0.66	0.0586
04 33 51.98	+22 50 30.3	17-OM-066	17-058	CI Tau	2	14.06 ± 0.08	48.00	0.19	0.0204
04 33 54.61	+26 13 26.8	18-OM-004	18-030	IT Tau AB	2	18.01 ± 0.05	1.25	6.49	0.4041
04 34 55.42	+24 28 52.7	25-OM-003	25-026	AA Tau	2	15.67 ± 0.18‡	0.45	1.24	0.0597
04 35 20.93	+22 54 23.4	08-OM-005	08-019	FF Tau AB	3	17.57 ± 0.03	1.89	0.80	0.0681
04 35 27.39	+24 14 58.5	12-OM-077	12-040	DN Tau	2	13.27 ± 0.04	98.91	1.15	0.1955
04 35 40.94	+24 11 09.2	12-OM-096	12-059	CoKu Tau 3 AB	3	20.58 ± 0.60	0.12	5.85	0.5224
04 35 41.80	+22 34 11.8	09-OM-070	09-022	KPNO-Tau 8	3	20.64 ± 0.04	0.11	0.50	0.0668
04 35 47.36	+22 50 20.6	08-OM-032	08-037	HQ Tau AB	3	15.01 ± 0.04	20.03	2.48	0.3050
04 35 51.10	+22 52 39.7	08-OM-034	08-043	KPNO-Tau 15	3	19.75 ± 0.13	0.25	2.62	0.2232
04 35 52.77	+22 54 22.7	08-OM-036	08-048	HP Tau AB	2	17.39 ± 0.04	2.22	2.55	0.1156
04 35 53.52	+22 54 08.6	08-OM-038	08-051	HP Tau/G3 AB	3	18.21 ± 0.07	1.05	1.29	0.0648
04 35 54.16	+22 54 12.9	08-OM-040	08-051	HP Tau/G2	3	13.63 ± 0.04	70.80	9.65	0.8136
04 35 56.84	+22 54 34.9	08-OM-044	08-058	Haro 6-28 AB	2	18.94 ± 0.12	0.53	0.25	0.0124
04 39 20.87	+25 45 02.8	05-OM-002	05-013	GN Tau AB	2	17.22 ± 0.11	2.61	0.79	0.0108
04 40 49.61	+25 51 19.2	07-OM-006	07-011	JH 223	3	18.25 ± 0.04	1.01	0.06	0.0131
04 42 05.46	+25 22 56.0	10-OM-002	10-017	CoKuLk332/G2 AB	3	18.68 ± 0.06	0.68	3.26	0.1826
04 42 07.33	+25 23 03.8	10-OM-003	10-018	CoKuLk332/G1 AB	3	19.09 ± 0.15	0.47	0.49	0.0470
04 42 07.77	+25 23 12.3	10-OM-004	10-020	V955 Tau AB	2	17.90 ± 0.08	1.39	1.62	0.0576
04 42 21.06	+25 20 34.1	10-OM-006	10-034	CIDA 7	2	18.67 ± 0.09	0.68	0.04	0.0028
04 42 37.66	+25 15 37.2	10-OM-010	10-045	DP Tau	2	15.84 ± 0.03	9.29	0.10[c]	0.0031

[a] U-band except if identified with † (*UVW1*) or ‡ (*UVW2*). [b] L_X (0.3 − 10 keV) in 10^{30} erg s^{-1} from the DEM method. [c] L_X (0.3 − 10 keV) of the hard component from Güdel et al. (2007b).

undetected in XEST-03, and once in "TMC X-ray outside OM FOV" since it fell off the OM detector in XEST-04.

Tables 5 and 6 repeat some of the columns in Table A.1 for TMC members and TMC candidates, respectively, but also provide the name of the TMC source (from Güdel et al. 2007a) or "(TMC cand)" (from Scelsi et al. 2007). The average OM count rate $Rate_{OM}$ (corrected for coincidence losses and aperture radius) is also given after calculation from the magnitude[2]. We used the zero-point magnitudes given in the *XMM-Newton* UHB (Z_U = 18.2593, Z_{UVW1} = 17.1882, Z_{UVW2} = 14.8026; Ehle et al. 2005). Note that this calibration does not take into account corrections specific to the source's spectral type. We also provide the X-ray luminosity L_X and X-ray count rate ($Rate_X$) from Güdel et al. (2007a).

[2] $\log Rate_{OM} = -0.4(m - Z)$, where m is the source's magnitude, and Z is the zero-point magnitude.

Table 6. XEST OM catalogue of TMC candidates detected in X-rays and in the OM.

RA_{corr}	δ_{corr}	XEST OM	XEST	Name	Mag[a]	$Rate_{OM}$	L_X^b	$Rate_X$
04 04 24.45	+26 11 12.0	06-OM-079	06-041	(TMC cand)	18.02 ± 0.05	1.25	7.3	17.1
04 14 52.31	+28 05 59.7	20-OM-010	20-071	(TMC cand)	19.87 ± 0.25	0.23	171	159
04 22 15.72	+26 57 05.3	11-OM-122	11-078	(TMC cand)	20.98 ± 0.14	0.08	23	9.4
04 22 27.29	+26 59 49.4	11-OM-150	11-088	(TMC cand)	20.11 ± 0.08	0.18	1.6	2.1
04 29 35.98	+24 35 57.0	13-OM-002	13-010	(TMC cand)	20.47 ± 0.23	0.13	68	22.1
04 29 36.29	+26 34 23.2	15-OM-093	15-034	(TMC cand)	18.70 ± 0.11	0.66	10	24.4
04 30 25.21	+26 02 56.9	14-OM-163	14-034	(TMC cand)	16.86 ± 0.01	3.62	0.35	0.8
04 33 33.07	+22 52 50.7	17-OM-028	17-043	(TMC cand)	20.66 ± 0.36	0.11	1.2	20.4
04 33 52.54	+22 56 27.0	17-OM-070	17-059	(TMC cand)	19.12 ± 0.06	0.45	40	57.4
04 33 55.64	+24 25 01.7	04-OM-044	04-060	(TMC cand)	17.30 ± 0.01	2.42	0.74	1.3
04 35 52.88	+22 50 57.8	08-OM-037	08-049	(TMC cand)	20.06 ± 0.21	0.19	115	118
04 35 58.93	+22 38 35.2	09-OM-143	09-042	(TMC cand)	15.37 ± 0.03	14.29	172	269

[a] U-band. [b] L_X (0.3–10 keV) in 10^{30} erg s^{-1} from the DEM method.

4. Properties of the OM Taurus sample

We focus in this section on some of the OM properties of the TMC sample as defined in Güdel et al. (2007a) that were detected in both X-rays and in the OM. Specifically, we focus on whether correlations can be found, e.g., between the X-ray luminosity and the OM magnitude, and on the U-band properties of weak-lined T Tau stars and classical T Tau stars. The low number of detections of type 1 sources is such that we will not discuss them.

Figure 2 shows the scatter plot of X-ray luminosities (as derived from the DEM method; see Güdel et al. 2007a) as a function of the observed OM magnitude (U-band or ultraviolet *UVW1* and *UVW2* bands). We used different symbols for the various types of stars. There is no strong evidence that any correlation exists in any type or any OM filter. However, at least one trend can be noticed: type 2 stars (usually CTTS) are overall *fainter* in X-rays than type 3 stars (usually WTTS). At a given OM magnitude, there is a wide range of X-ray luminosities below 10^{31} erg s^{-1} in type 2 stars. Figure 3 shows the cumulative distribution of X-ray count rates in type 2 and 3 stars that were detected in both OM and X-rays. A Kolmogorov-Smirnov (K-S) test gives a significance level of $P = 0.0055$ that both distributions are compatible ($D = 0.49$; the D statistic is the maximum vertical deviation between the two curves), indicating that the two cumulative distributions differ at a high significance level. This result is discussed in detail in Güdel et al. (2007a) and Telleschi et al. (2007a).

Despite the clear difference in X-ray luminosity between type 2 and 3 stars, there is little evidence that the observed OM magnitude of type 2 stars are much different from those of type 3 stars (Fig. 4). Indeed, a K-S test gives a significance level of $P = 0.54$ ($D = 0.25$). If the observed OM magnitudes scale with L_*, then the similar distributions for type 2 and 3 stars would not be surprising, and again, we would find the CTTS to be fainter only in the X-rays (Fig. 3), pointing at a true deficiency of emission in that wavelength range (Telleschi et al. 2007a). However, it is important to keep in mind that the observed magnitudes could be biased by certain factors. Therefore, we aim to test the following hypotheses that could produce an observational bias: I) Bolometric luminosities in type 2 and type 3 stars are different; II) The binary fraction is higher in one object type than another; III) Extinction in the U band is stronger for one type than for the other; IV) One object type has a significant excess in the U-band.

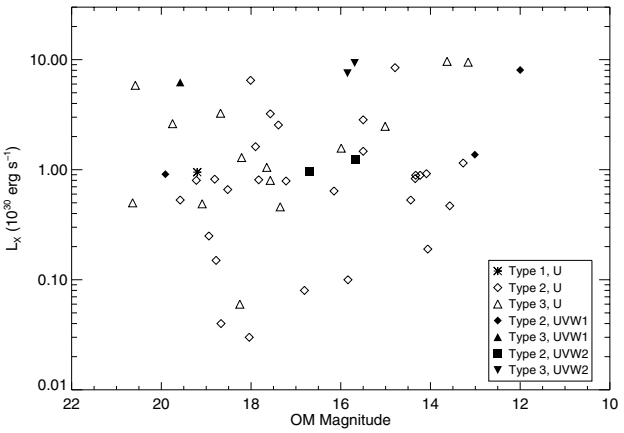

Fig. 2. X-ray luminosity (L_X) in 10^{30} erg s^{-1} as a function of the observed OM magnitude. Various types of stars are identified (see text). Ultraviolet magnitudes are identified with filled symbols.

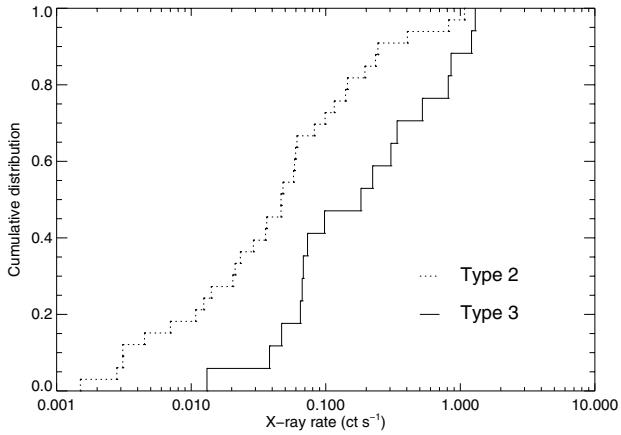

Fig. 3. Cumulative distributions of X-ray count rates of type 2 and 3 stars.

4.1. Hypothesis I

Figure 5 shows the cumulative distribution of the star's luminosity (see Güdel et al. 2007a) for type 2 and 3 stars detected in the U band. Note that we used the luminosity of the primary component if available for multiples (Table 9 in Güdel et al. 2007a). There is no evidence that the stellar luminosity

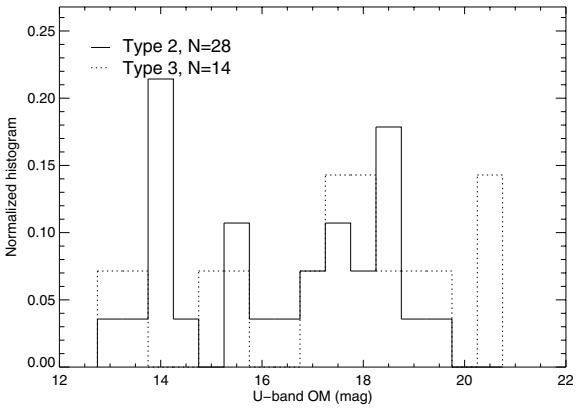

Fig. 4. Histogram of OM U magnitudes for type 2 and 3 stars.

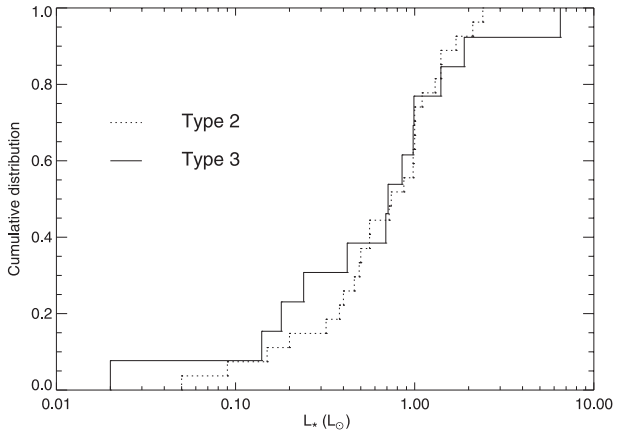

Fig. 5. Cumulative distributions of stellar luminosity of type 2 and 3 objects detected in the U filter.

of type 2 stars is different from that of type 3 stars, as indicated by the high significance of a K-S test ($D = 0.16, P = 0.97$). Therefore, hypothesis I can be safely rejected as a potential biasing factor.

4.2. Hypothesis II

In our OM U-band sample, there are 14 and 9 TMC stars of type 2 and 3, respectively, with more than 1 component. Therefore, we created cumulative distributions of the OM magnitude for the remaining single components (14 and 5 stars for type 2 and 3, respectively): There is no evidence of a difference in the OM magnitudes for single type 2 and 3 stars (K-S test: $D = 0.37, P = 0.58$). Therefore, hypothesis II is also rejected.

4.3. Hypothesis III

We used extinction magnitudes in the J band (A_J) if available, and determined the A_U magnitudes. Our procedure was the following: first, we calculated A_J/A_V and A_U/A_V ratios based on coefficients given by Cardelli et al. (1989): $A_J/A_V = 0.4008–0.3679/R_V$ and $A_U/A_V = 0.9530 + 1.9090/R_V$, where we used $R_V = 5.5$. Indeed such a value gives a better fit of the observed

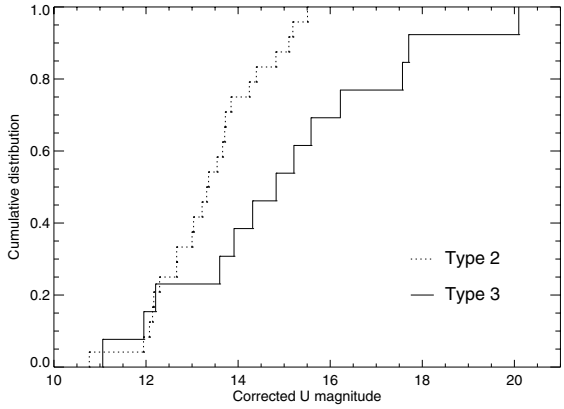

Fig. 6. Cumulative distributions of U-band OM magnitudes after correction for extinction. Type 2 stars have brighter OM magnitudes than type 3 stars. Stars with known $T_{\rm eff}$ and A_J are shown.

A_J/A_V values[3]. Then, we calculate the estimated extinction magnitude in the U band, A_U:

$$A_U = \frac{A_U}{A_V}\frac{A_V}{A_J}A_J.$$

We obtained the distributions of A_U for type 2 and 3 stars observed with the OM in the U band. Unexpectedly, the cumulative distributions do not differ significantly. To verify this finding, we calculated A_U from A_V ($A_U = \frac{A_U}{A_V}A_V$) and found the same result. Since A_V is more subject to optical veiling than A_J, we preferred to use A_U obtained from A_J in this paper.

Although the distributions of extinction magnitudes are overall similar in our sample, we have noticed that they are correlated with the observed U-band magnitude in type 2 stars, but not in type 3 stars. It appears that, in our sample, type 2 stars with fainter U magnitudes suffer from more extinction than brighter type 2 stars. Therefore, we have used the above A_U to correct the observed OM U-band magnitudes and we constructed the cumulative distribution (Fig. 6). The distributions are significantly different, with type 2 stars being much brighter in the U-band than type 3 stars (K-S statistic $D = 0.44$ with a significance level P of 0.05).

Therefore, hypothesis III appears to be correct in the sense that type 2 stars are brighter in the U-band but suffer more extinction than type 3 stars, as could be expected based on observed properties of young stars. We emphasize, however, that this trend is opposite to the trend in X-rays where CTTS are *fainter*. Nevertheless, as shown earlier, both types of stars have similar stellar luminosities, indicating that there must be a U-band excess in type 2 stars. Therefore, we need to address hypothesis IV before we can draw any firm conclusion.

4.4. Hypothesis IV

To determine the U-band excesses, we used the distance modulus ($m - M = 5.73$ for a distance to the TMC of 140 pc) to calculate the corrected absolute U-band magnitude, M_U, from the observed extinction-corrected U magnitude. We then determined the stellar photospheric absolute U magnitude tabulated by Siess et al. (2000) (that use a $Z = 0.02$ metallicity and the

[3] When more than one extinction magnitude was available for multiples, we used the value from the primary.

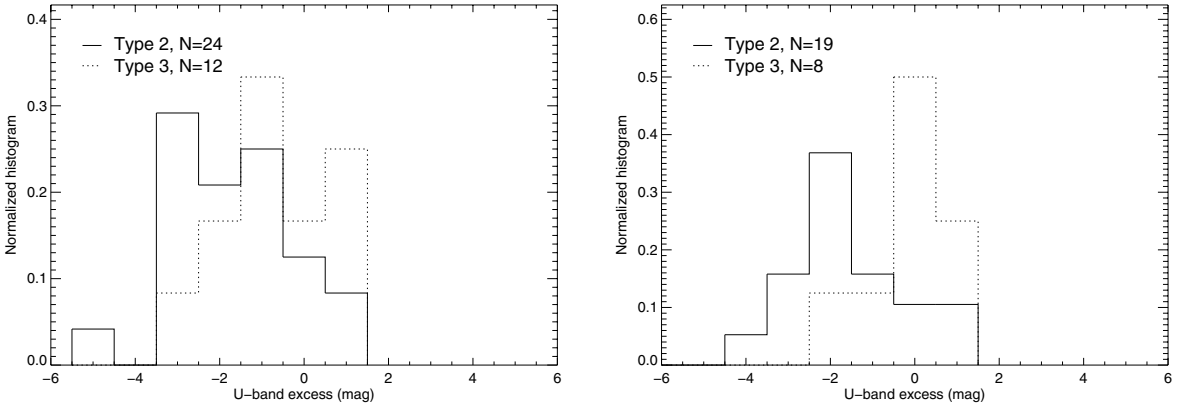

Fig. 7. Normalized distributions of U-band excesses for type 2 and 3 stars. Excesses determined when A_J was used to calculate A_U are shown in the *left* figure, whereas excesses determined with A_V used are shown in the *right* figure.

conversion table of Kenyon & Hartmann 1995). We finally compared the stellar photospheric M_U with the observed extinction-corrected absolute U magnitude. Figure 7 shows the normalized histograms of the U-band excesses. We provide distributions determined from A_U that was calculated either from A_J (left figure) or A_V (right figure). The distributions of excesses are different, as shown from Kolmogorov-Smirnov tests of the cumulative distributions of excesses that give very low probabilities ($P = 0.16$ and $P = 0.04$ for excesses derived from A_J and A_V, respectively). Type 2 stars generally show a U-band excess of 0–3 mag, whereas type 3 stars either show no excess or slight U-band deficiency. There are exceptions for stars of both types, probably due to inaccurate background subtraction (mostly due to the central ghost emission at the center of the OM image), inaccurate extinction correction, binary effects, or a lower than expected count rate in bright stars due to instrumental effects (fixed pattern noise).

In conclusion, we have shown that binarity and stellar luminosity in our sample do not bias the observed OM magnitudes. However, although the extinction magnitudes are statistically similar in type 2 and 3 stars, they are correlated in type 2 stars with the observed magnitudes. After correction for extinction, type 2 stars are found to be brighter than type 3 stars, which can be explained by a U-band excess due to accretion.

5. Optical and X-ray light curves

Figure B.1 presents the collection of simultaneous X-ray and optical/UV light curves of XEST sources detected in both X-rays and in the OM. The X-ray light curves are shown on the top panel with the XEST identification, while the OM light curve is shown in the bottom panel with the XEST-OM identification. The OM light curves are taken from the IMAGING mode data only. The x-axis OM error bars correspond to the length of an exposure identification. If a TMC member is associated with the source, its name is given next to the XEST or XEST-OM identification. Special cases occur, e.g., when two nearby sources were not separated in X-rays but they were in the OM. For example, the X-ray light curve of XEST-19-049 is associated with both UZ Tau E and W, whereas we manually extracted (due to problems in the SAS software to properly extract both sources due to the close separation) the OM light curves for UZ Tau W (AB) and UZ Tau E (XEST-19-OM-092 and XEST-19-OM-094, respectively)[4]. A similar case is reported for HP Tau/G3 AB and HP Tau/G2 (XEST-08-051). The X-ray light curve, although dominated by HP Tau/G2, has some contribution (about 8%; see Telleschi et al. 2007a) from HP Tau/G3 AB. In contrast, the OM cleanly separated their emission (HP Tau/G3 AB = XEST-08-OM-038; HP Tau/G2 = XEST-08-OM-40). TMC candidates (Scelsi et al. 2007) are identified as well. X-ray and OM sources presently not identified as either TMC member or TMC candidate only have their XEST and XEST-OM identifications.

As mentioned earlier, our database includes several cases where only a few OM points were available for a specific target (e.g., CoKu Tau 3 AB; CW Tau; CIDA 1, etc.). However, there are several cases for which we have very good coverage even with the OM IMAGING data (e.g., FM Tau; V773 Tau ABC; CIDA 7; etc.). DG Tau A (XEST-02-022 = XEST-02-OM-028) is a good example where even low time resolution was able to catch the U-band emission of a flare, which peaked before the peak in the X-rays, a signature of the Neupert effect. Güdel et al. (2007b) give a full analysis of the DG Tau A case and make use of the OM light curve.

In addition, some OM data were obtained in FAST mode, allowing us to obtain high time resolution light curves. Figure 8 shows the OM FAST light curves together with the X-ray light curves. The classification type is also given on the upper right corner of each panel. The light curve of T Tau will be presented elsewhere (Güdel et al. 2007c). The OM FAST data of IT Tau and UZ Tau EW were not useful since the sources fell on or slightly outside the OM FAST window, and thus the light curves

[4] The OM light curves were obtained by manually determining the position of the two stars in each exposure image, and then using an IDL routine to extract the light curve. We used radii of half the stars' separation (3.″48, i.e., a radius of 3.65 pixels for the central window), which minimizes the contamination of one source onto the second one. We corrected for aperture, applied the theoretical and empirical corrections, corrected for deadtime, and applied a time-dependent sensitivity correction. The above procedure is similar to what the SAS task *omsource* does; however, the latter cannot yet extract for radii lower than 6 pixels. We defined an annulus of radii 20 and 30 pixels (≈10″ and 15″) for the local background contribution. See Grosso et al. (2007a) for a detailed description of the procedure.

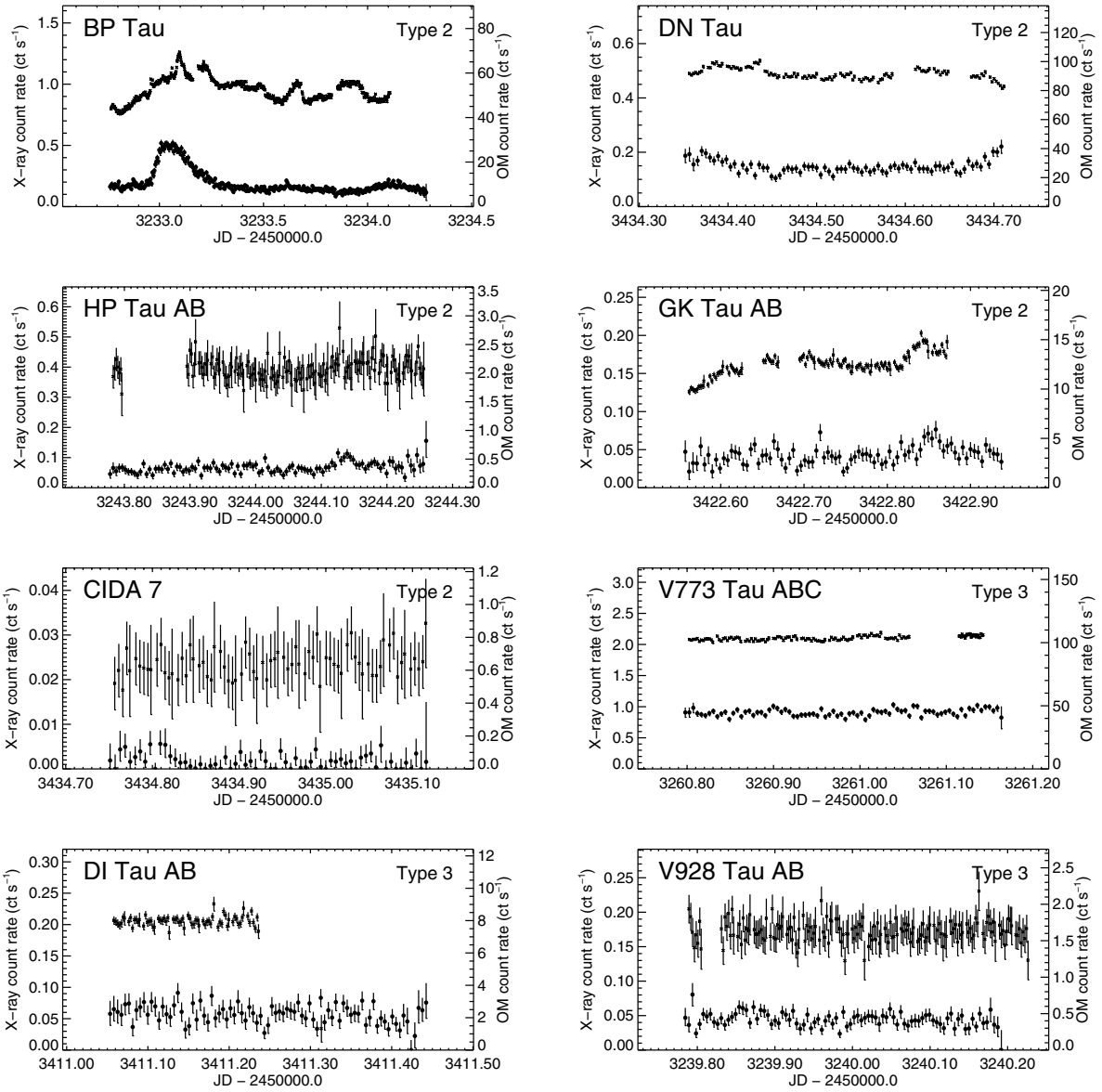

Fig. 8. The TMC sample of stars with OM FAST mode data. The upper curve in each panel is the OM light curve (*right y*-axis), whereas the lower curve is the X-ray light curve (*left y*-axis). The OM light curves were rebinned to bin sizes of 200 s, except for CIDA 7, which required a bin size of 400 s. The type of the source is given together with the source name. The OM FAST data of IT Tau and UZ Tau EW are not shown since the sources were not properly placed on the small OM FAST window, and thus the light curves were unreliable. In addition, the T Tau OM FAST light curve is the subject of a separate paper and will be presented elsewhere (Güdel et al. 2007c). Note that small manual corrections were necessary for DN Tau, DI Tau AB, and BP Tau (see footnote 5).

are not reliable. We also applied some manual corrections to the OM FAST light curves of DN Tau, DI Tau, and BP Tau[5].

Focusing on the OM FAST light curves, it is clear that type 3 stars show almost no variability in the OM, in contrast to type 2 stars. The classical T Tau star BP Tau shows significant UV variability (the BP Tau data were originally presented

[5] In the case of DN Tau, due to a feature in SAS 6.x, about half the counts were processed in the exposure S009 (DATE-OBS = "2005-03-05T01:37:35" and DATE-END = "2005-03-05T02:02:35") only. The average count rate in this exposure is 37.7 ct s^{-1}, after correction for deadtime, aperture, and coincidence losses. The detected count rate for S009 is 32.2 ct s^{-1} (i.e., 1.17 times smaller), based on the theoretical correction in the *XMM-Newton* Users Handbook (the empirical correction is minimal). In contrast, the average count rate in the preceding exposure (S408) is 87.7 ct s^{-1}. The latter corresponds to a detected count rate of 63.4 ct s^{-1} (i.e., 1.38 times smaller). Thus, we multiplied the count rates in S009 by $2/1.17 \times 1.38 = 2.36$ to correct for the SAS feature. For DI Tau, the pointing of the satellite changed unexpectedly after DATE-OBS = "2005-02-09T19:30:13" (exposures S412, S009, S413-S416), and DI Tau fell just on the edge of the OM FAST window. We thus discarded count rates after this epoch. For BP Tau, a problem with the time stamps of exposure S051 occurred. The DATE-OBS and DATE-END keywords of the following exposure, S052, were incorrectly used, and thus the time stamps of events were incorrectly calculated by the SAS software. We manually corrected these time stamps and keywords by using the correct keywords, DATE-OBS = "2004-08-16T06:45:56" DATE-END = "2004-08-16T08:27:51", and incidentally shifting the time stamps by −6256 s. The same timing problem for the S051 IMAGING data of BP Tau needed a similar correction of the date keywords.

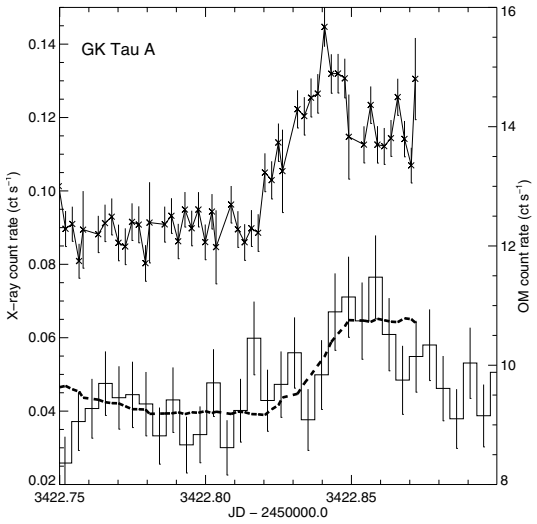

Fig. 9. Details of the GK Tau OM and X-ray light curves. The OM light curve (top curve) was rebinned to a bin size of 200 s, while the X-ray light curve (bottom histogram) used a 400 s bin size. The thick dashed line corresponds to the OM light curve convolved through a kernel $K(t, t')$ (see text) but it was shifted down for clarity. The GK Tau A event shows evidence of a Neupert-like effect.

by Schmitt et al. 2005). One large X-ray flare is visible at the start of the observation, with two slowly varying flux enhancements that could be due to flares, but also rotational modulation of bright active regions. The *UVW1* light curve of BP Tau does not show direct evidence of correlations with the X-ray light curve. In fact, the UV flux peaks *after* the X-ray light curve, in contradiction with the Neupert effect paradigm. However, such a peculiar behavior is not uncommon in some flares observed in the Sun or in main-sequence or evolved magnetically active stars with no accretion (e.g., Ayres et al. 2001; Stelzer et al. 2003; Osten et al. 2005). Nevertheless, the strong variability in the OM light curve is generally uncorrelated with the X-ray light curve, which strongly suggests that the OM light curve is completely dominated by the UV emission of accretion spots in BP Tau. The period of BP Tau being 7.60 d, much longer than the 1.5 d duration of the observation or typical OM "events" (0.1–0.2 d), it is more probable that such events are due to accretion events such as those observed in the brown dwarf 2MASS J04141188+2811535 (Grosso et al. 2007a).

The GK Tau light curves deserve special attention. Indeed, the OM light curve shows evidence of two behaviors: a general slow variation uncorrelated with the X-ray light curve that is probably due to the rotational modulation of accretion spots (P = 4.60 d), and a short-duration event around JD 2453422.84 that appears related to a small flare-like event in the X-rays. Figure 9 shows an extract of the light curves. Note that the OM emission is from GK Tau A. The companion at 2.″5 was not detected in the OM. In the X-rays, the binary cannot be resolved; nevertheless, the A component should contribute the most to the X-ray emission. In addition, the X-ray emission is blended with the X-ray emission of the nearby GI Tau. The X-ray light curves of GK Tau AB and GI Tau shown in this paper take into account this blend since they were extracted from smaller radii (160 pix, i.e., 8″). We convolved the OM light curve through the kernel function, $K(t, t')$, where $K(t, t') = \mathrm{e}^{-(t-t')/\tau}$ if $t' < t$ and $K(t, t') = 0$ otherwise, and where τ was set to 2 ks; for clarity and comparison with the X-ray light curve, we introduced a vertical offset to the convolved light curve. The convolution of the OM light curve is similar to an integration; however, the use of the exponential function in the kernel allows us to mimic the decaying effect of radiative and conductive cooling in X-rays. This exercise is a good indication that the event observed in X-rays and in the OM in GK Tau is a flare that displayed a Neupert-like effect, with the optical emission peaking before the X-rays. A similar case is reported in DG Tau A with OM IMAGING data (Güdel et al. 2007b). GK Tau's OM light curve can, therefore, be seen as a combination of stellar photospheric emission, accretion spot emission producing slow variability, and flare-like events. As seen from GK Tau, but most visibly BP Tau (and other type 2 stars), the long-term variability due to accretion does not appear to correlate with the X-ray variability in general. This indicates that the contribution of accretion to the X-ray emission is limited, probably to the soft component only, as suggested from high-resolution X-ray spectra of classical T Tau stars (Telleschi et al. 2007a). In contrast, type 3 stars with little or no accretion do not show evidence of slow variability in the OM.

6. Summary and conclusions

We have presented results from the Optical Monitor data of the *XMM-Newton* Extended Survey of the Taurus Molecular Cloud. Optical (U) or ultraviolet (*UVW1* or *UVW2*) magnitudes were obtained; in addition low time resolution light curves from the IMAGING data were compiled and compared to the X-ray light curves. For a few sources, FAST mode data with high time resolution were available as well.

The OM data are unique since they provide strictly simultaneous coverage in the optical (or ultraviolet) together with X-rays. This *XMM-Newton* capability allowed us to study light curves; we were able to detect Neupert-like effects in the accreting stars GK Tau A and DG Tau A, but also slow variability in accreting stars that is most likely due to accretion spots. A statistical analysis shows that, although observed U magnitudes are similar in type 2 and 3 stars, accreting stars are, in fact, brighter in the U band than type 3 stars after correction for extinction. This excess emission most likely originates from accretion. This behavior, although not a new discovery, is now shown to be disconnected from the X-ray variability. Indeed, for example, the light curve of BP Tau shows strong ultraviolet variability that is not reproduced in the X-ray light curve. In contrast, non-accreting stars (or stars with low accretion rates) do not show evidence of slow variability. Their emission is therefore probably dominated by photospheric emission. Similar results were found in the optical (*BVRI*) and X-ray data of Orion Nebula Cluster pre-main sequence stars (Stassun et al. 2006).

The XEST OM catalogue lists 2 148 detected sources and about 88% (1893) OM sources had 2MASS counterparts; in contrast, 916 sources were detected in the X-rays and had coordinates such that they could be detected in the OM (not necessarily). However, only 98 X-ray sources matched OM sources, after astrometric corrections applied to both the X-rays and the OM coordinates based on 2MASS coordinates. Of these 98 sources, only 51 are considered as TMC members (12 are bona-fide TMC candidates; Scelsi et al. 2007). Therefore, the vast majority (about 97%) detected in the OM images are, in fact, not TMC members. While it is hard to determine the origin of a target based on X-ray or optical data alone, the OM data, together with 2MASS and *Spitzer* data (Padgett et al. 2006, in preparation), should provide useful constraints to discriminate between stellar and non-stellar objects, and thus discover new members of the Taurus Molecular Cloud.

Acknowledgements. We thank the anonymous referee for detailed comments and suggestions that helped to improve this manuscript. M. A. acknowledges support by National Aeronautics and Space Administration (NASA) grant NNG05GF92G and from a Swiss National Science Foundation Professorship (PP002–110504). L. S. ackoweldges financial contribution from contract ASI-INAF I/023/05/0 and M.I.U.R. We acknowledge financial support by the International Space Science Institute (ISSI) in Bern to the *XMM-Newton* XEST team. The PSI group was supported by the Swiss National Science Foundation (grants 20-66875.01 and 20-109255/1). Part of this research is based on observations obtained with *XMM-Newton*, an ESA science mission with instruments and contributions directly funded by ESA member states and the USA (NASA). This publication makes use of data products from the Two Micron All Sky Survey (2MASS), which is a joint project of the University of Massachusetts and the Infrared Processing and Analysis Center/California Institute of Technology, funded by NASA and the National Science Foundation. Our research made use of the SIMBAD database, operated at CDS, Strasbourg, France.

References

Antonucci, E., Gabriel, A. H., & Dennis, B. R. 1984, ApJ, 287, 917
Audard, M., Güdel, M., Skinner, S. L., et al. 2005, ApJ, 635, L81
Ayres, T. R., Brown, A., Osten, R. A., et al. 2001, ApJ, 549, 554
Bouvier, J. 1990, AJ, 99, 946
Bouvier, J., & Bertout, C. 1989, A&A, 211, 99
Bouvier, J., Bertout, C., & Bouchet, P. 1988, A&AS, 75, 1
Bouvier, J., Cabrit, S., Fernandez, M., Martin, E. L., & Matthews, J. M. 1993, A&A, 272, 176
Bouvier, J., Covino, E., Kovo, O., et al. 1995, A&A, 299, 89
Bouvier, J., Wichmann, R., Grankin, K., et al. 1997, A&A, 318, 495
Cardelli, J. A., Clayton, G. C., & Mathis, J. S. 1989, ApJ, 345, 245
Ehle, M., et al. 2005, *XMM-Newton* Users' Handbook (v2.3)
Flaccomio, E., Micela, G., Sciortino, S., et al. 2005, ApJS, 160, 450
Grosso, N., Kastner, J. H., Ozawa, et al. 2005, A&A, 438, 159
Grosso, N., Audard, M., Bouvier, J., Briggs, K. R., & Güdel, M. 2007a, A&A, 468, 557
Grosso, N., Briggs, K. R., Güdel, M., et al. 2007b, A&A, 468, 391
Güdel, M., Benz, A. O., Schmitt, J. H. M. M., & Skinner, S. L. 1996, ApJ, 471, 1002
Güdel, M., Audard, M., Skinner, S. L., & Horvath, M. I. 2002a, ApJ, 580, L73
Güdel, M., Audard, M., Smith, K. W., et al. 2002b, ApJ, 577, 371
Güdel, M., Audard, M., Reale, F., Skinner, S. L., & Linsky, J. L. 2004, A&A, 416, 713
Güdel, M., Skinner, S. L., Briggs, K. R., et al. 2005, ApJ, 626, L53
Güdel, M., Briggs, K. R., Arzner, K., et al. 2007a, A&A, 468, 353
Güdel, M., Telleschi, A., Audard, M., et al. 2007b, A&A, 468, 515
Güdel, M., Skinner, S. L., Mel'nikov, S. Y., et al. 2007c, A&A, 468, 529
Hawley, S. L., Fisher, G. H., Simon, T., et al. 1995, ApJ, 453, 464
Hawley, S. L., Allerd, J. C., Johns-Krull, C. M., et al. 2003, ApJ, 597, 535
Herbst, W., Herbst, D. K., Grossman, E. J., & Weinstein, D. 1994, AJ, 108, 1906
den Herder, J. W., Brinkman, A. C., Kahn, S. M., et al. 2001, A&A, 365, L7
Jansen, F., Lumb, D., Altieri, B., et al. 2001, A&A, 365, L1
Kastner, J. H., Huenemoerder, D. P., Schulz, N. S., Canizares, C. R., & Weintraub, D. A. 2002, ApJ, 567, 434
Kastner, J. H., Richmond, M., Grosso, N., et al. 2004, Nature, 430, 429
Kastner, J. H., Franz, G., Grosso, N., et al. 2005, ApJS, 160, 511
Kastner, J. H., Richmond, M., Grosso, N., et al. 2006, ApJ, 648, L43
Kenyon, S. J., & Hartmann, L. 1995, ApJS, 101, 117
Luhman, K. L. 2004, ApJ, 617, 1216
Mason, K. O., Breeveld, A., Much, R., et al. 2001, A&A, 365, L36
Mitra-Kraev, U., Harra, L. K., Güdel, M., et al. 2005, A&A, 431, 679
Ness, J.-U., & Schmitt, J. H. M. M. 2005, A&A, 444, L41
Neupert, W. M. 1968, ApJ, 153, L59
Osten, R. A., Hawley, S. L., Allred, J. C., Johns-Krull, C. M., & Roark, C. 2005, ApJ, 621, 398
Robrade, J., & Schmitt, J. H. M. M. 2006, A&A, 449, 737
Rydgren, A. E., & Vrba, F. J. 1983, ApJ, 267, 191
Rydgren, A. E., Zak, D. S., Vrba, F. J., Chugainov, P. F., & Zajtseva, G. V. 1984, AJ, 89, 1015
Scelsi, L., Maggio, A., Micela, G., et al. 2007, A&A, 468, 405
Schmitt, J. H. M. M., Robrade, J., Ness, J.-U., Favata, F., & Stelzer, B. 2005, A&A, 432, L35
Siess, L., Dufour, E., & Forestini, M. 2000, A&A, 358, 593
Smith, K., Güdel, M., & Audard, M. 2005, A&A, 436, 241
Stassun, K. G., van den Berg, M., Feigelson, E., & Flaccomio, E. 2006, ApJ, 649, 914
Stelzer, B., & Schmitt, J. H. M. M. 2004, A&A, 418, 687
Stelzer, B., Fernández, M., Costa, V. M., et al. 2003, A&A, 411, 517
Strüder, L., Briel, U., Dennerl, K., et al. 2001, A&A, 365, L18
Swartz, D. A., Drake, J. J., Elsner, R. F., et al. 2005, ApJ, 628, 811
Telleschi, A., Güdel, M., Briggs, K. R., Audard, M., & Scelsi, L. 2007a, A&A, 468, 443
Telleschi, A., Güdel, M., Briggs, K. R., et al. 2007b, A&A, 468, 541
Turner, M. J. L., Abbey, A., Arnaud, M., et al. 2001, A&A, 365, L27
Vrba, F. J., Rydgren, A. E., Chugainov, P. F., Shakovskaia, N. I., & Zak, D. S. 1986, ApJ, 306, 199
Vrba, F. J., Rydgren, A. E., Chugainov, P. F., Shakovskaia, N. I., & Weaver, W. B. 1989, AJ, 97, 483
Vrba, F. J., Chugainov, P. F., Weaver, W. B., & Stauffer, J. S. 1993, AJ, 106, 1608

Online Material

Appendix B: X-ray and OM light curves

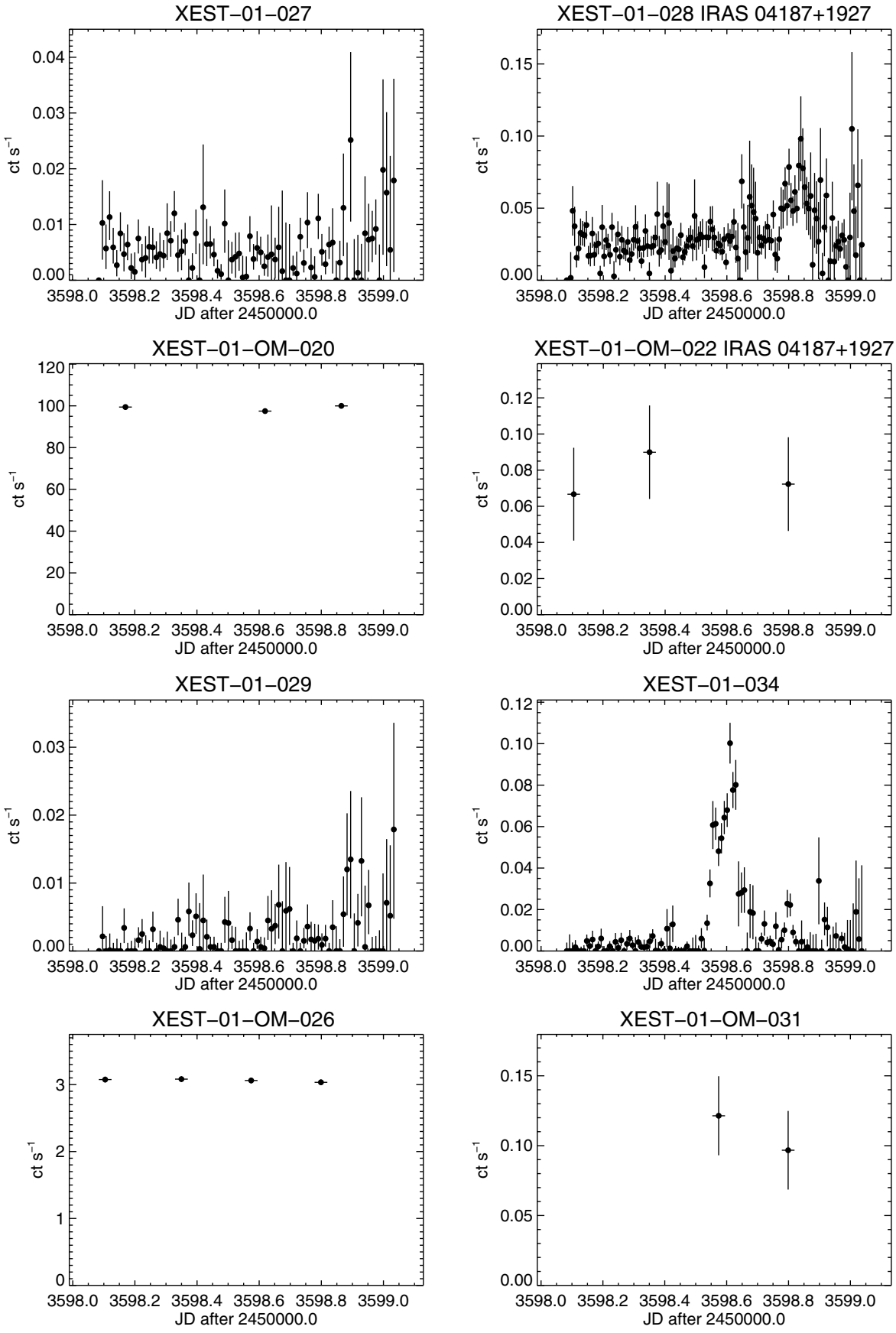

Fig. B.1. Light curves.

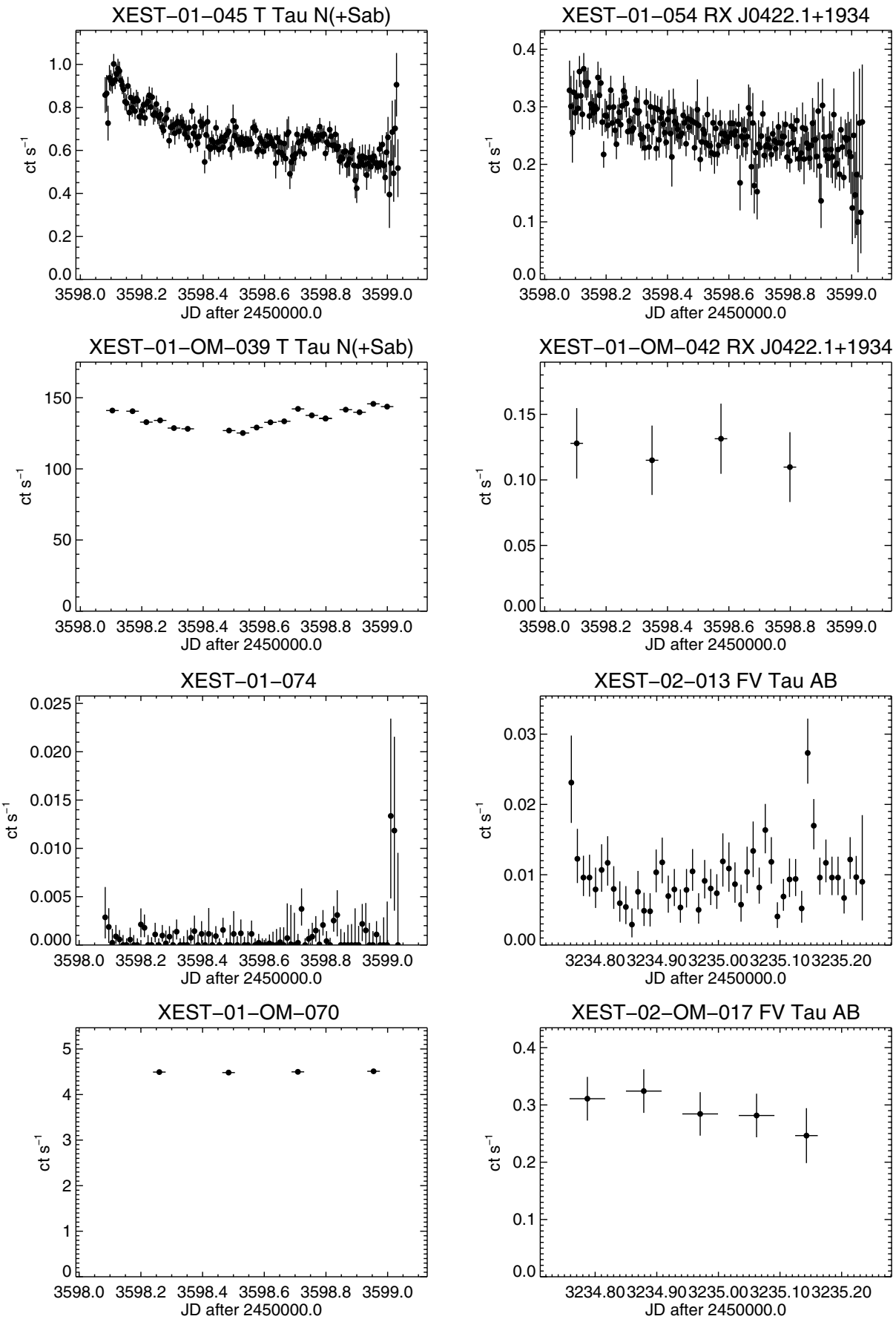

Fig. B.1. continued.

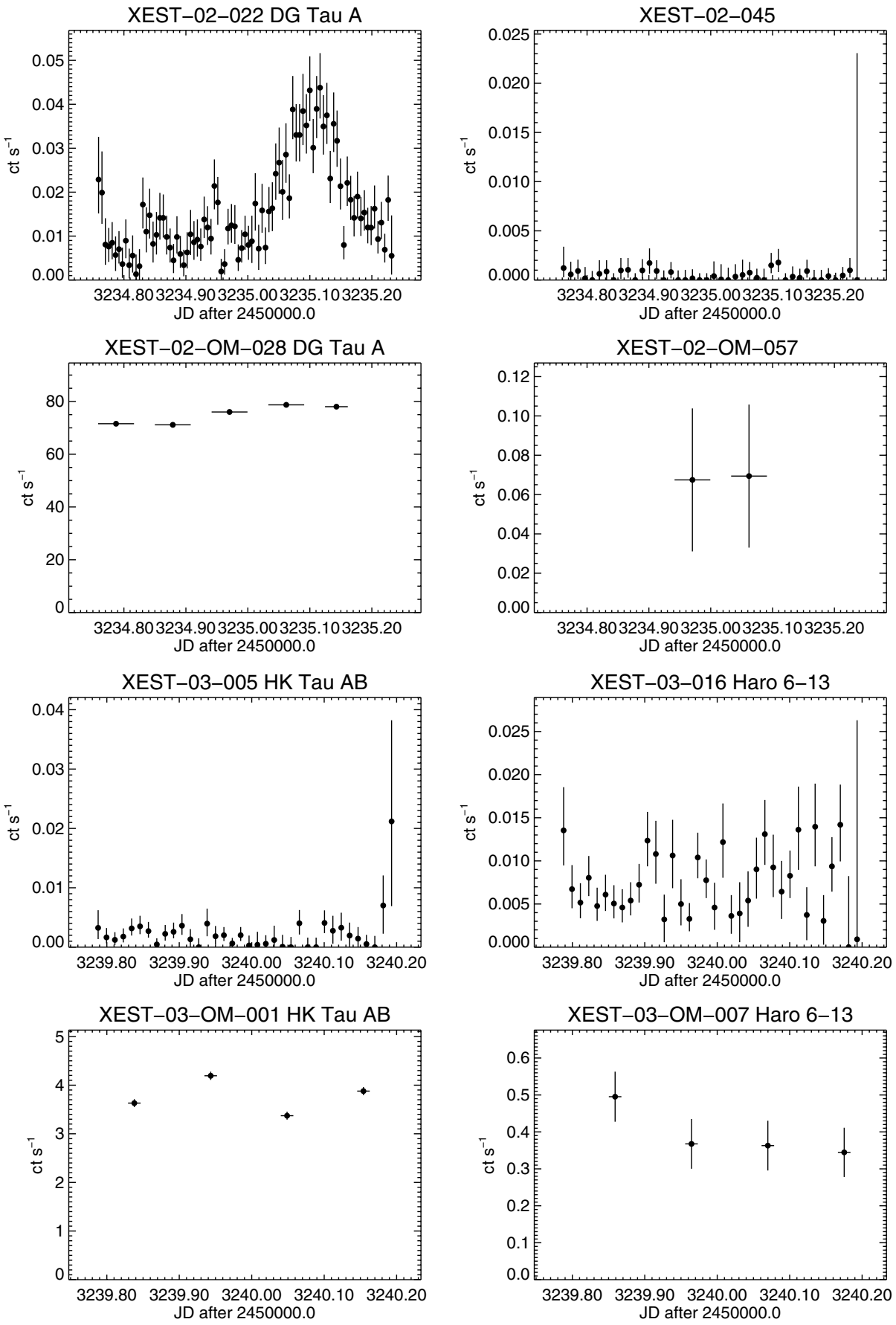

Fig. B.1. continued.

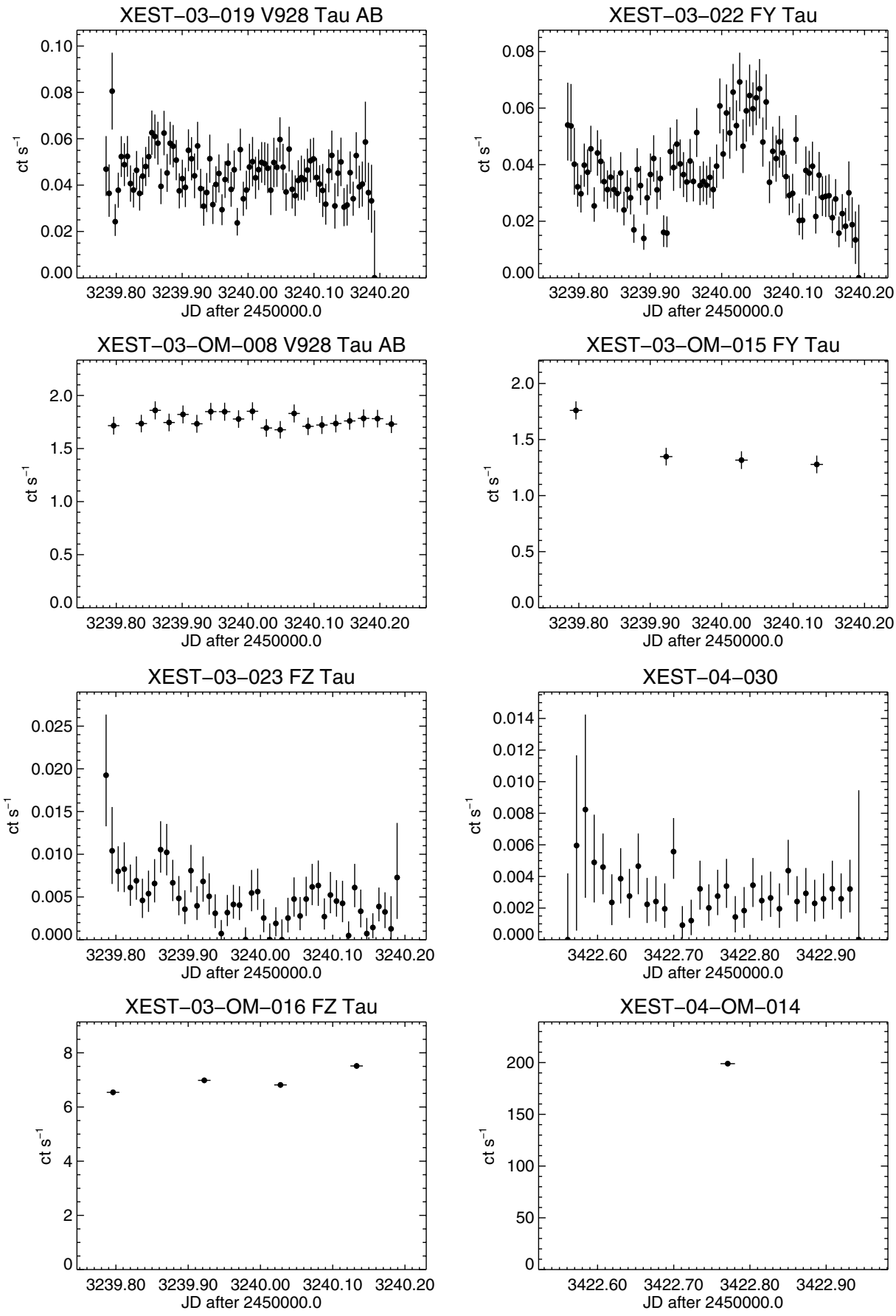

Fig. B.1. continued.

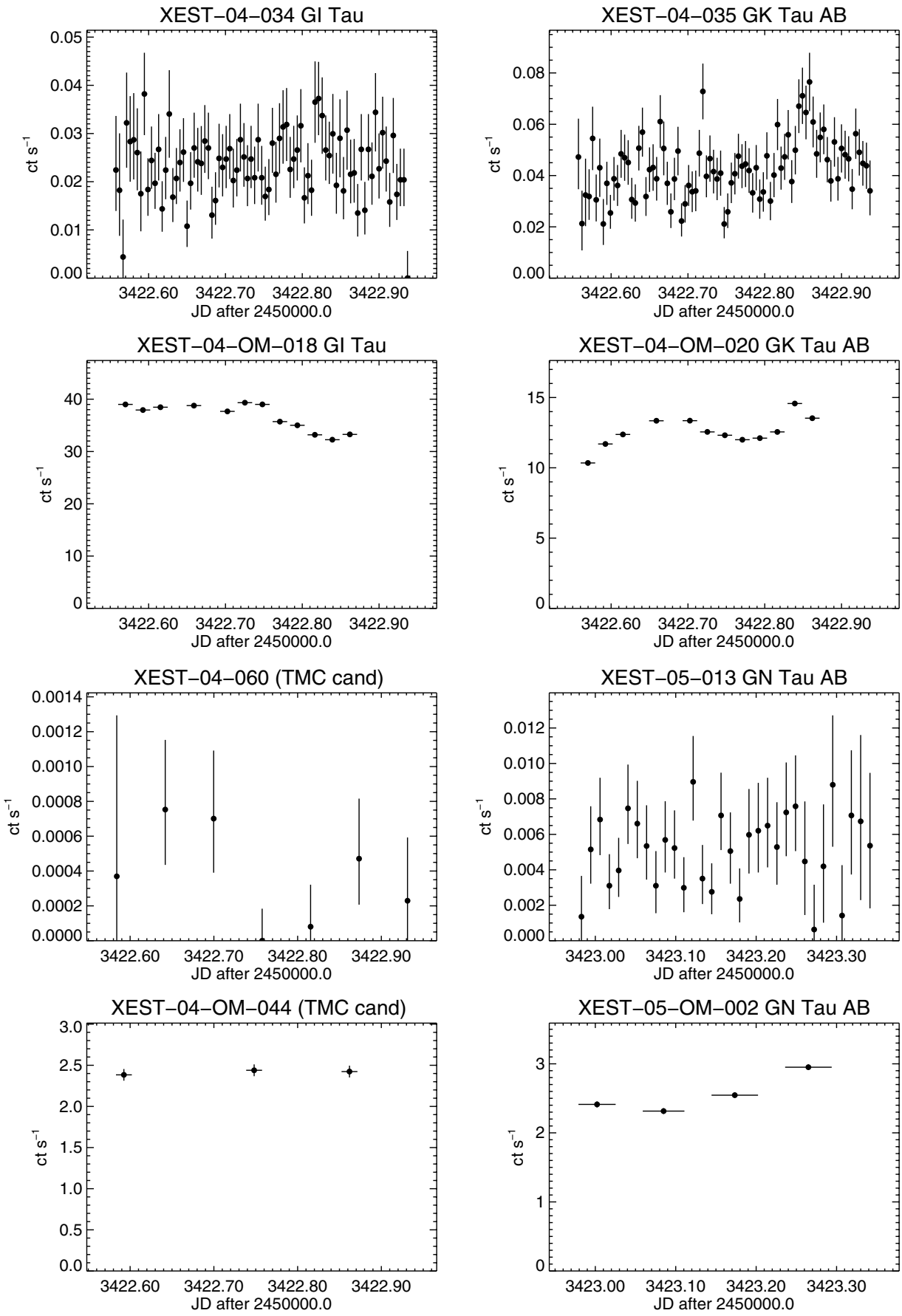

Fig. B.1. continued.

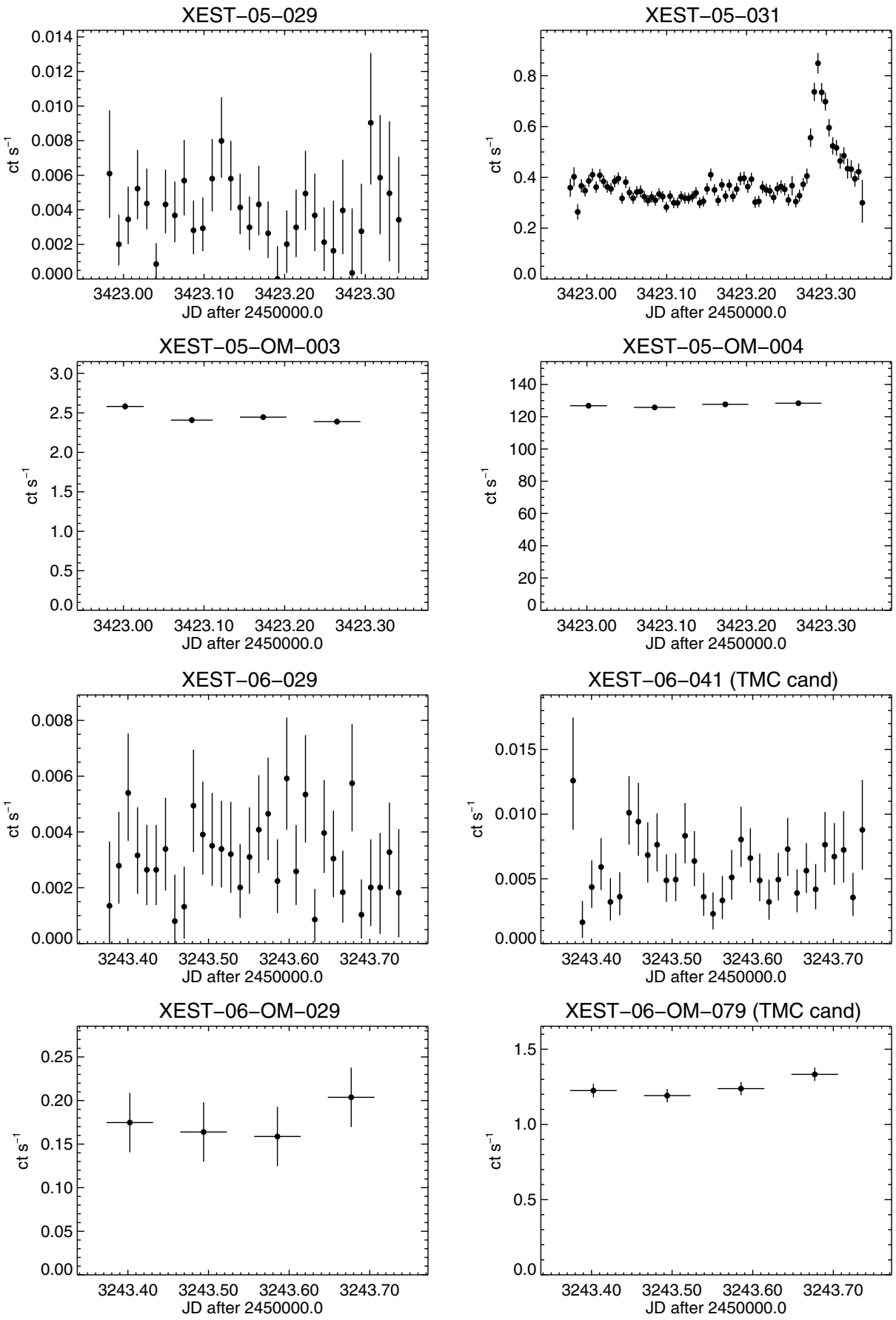

Fig. B.1. continued.

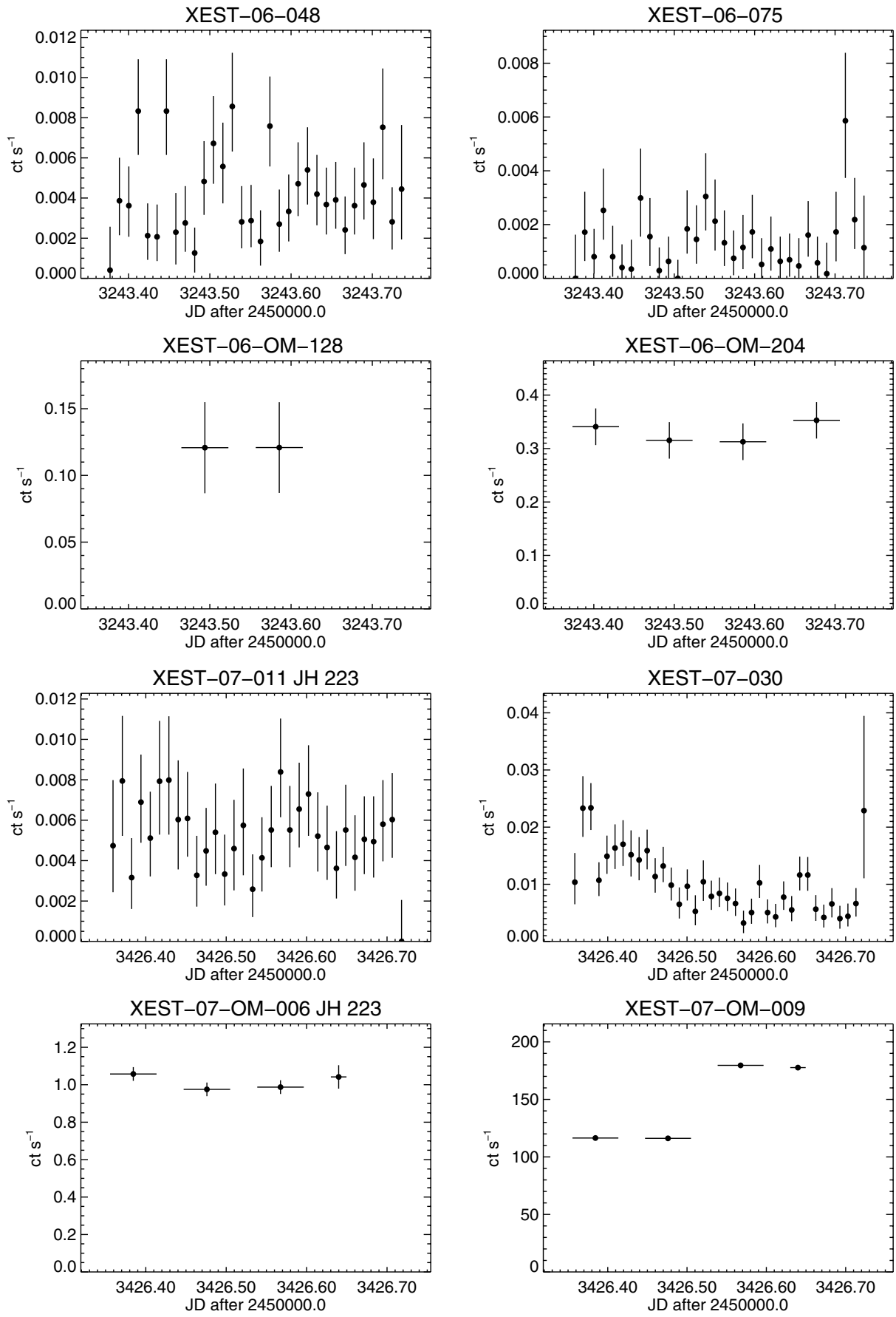

Fig. B.1. continued.

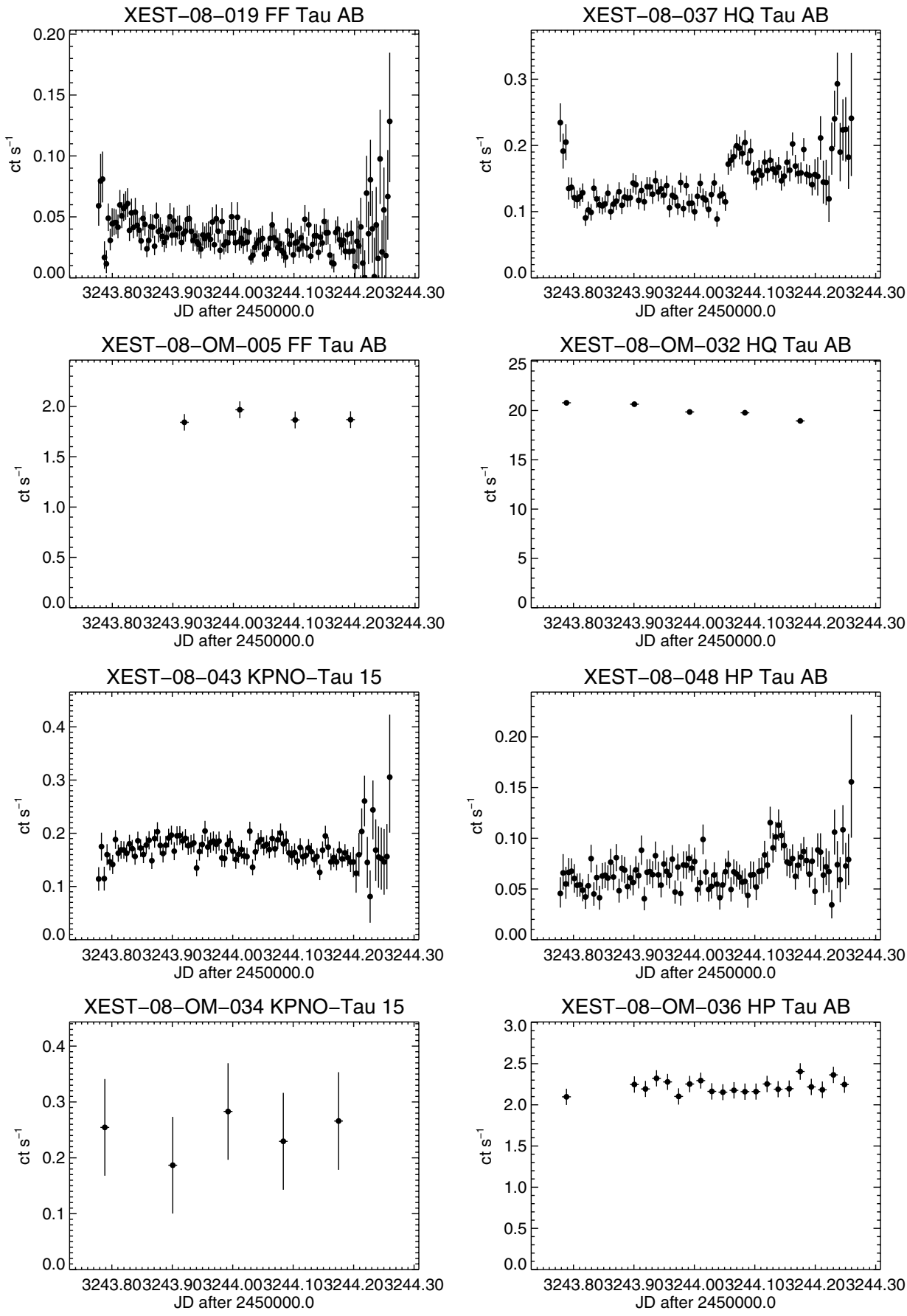

Fig. B.1. continued.

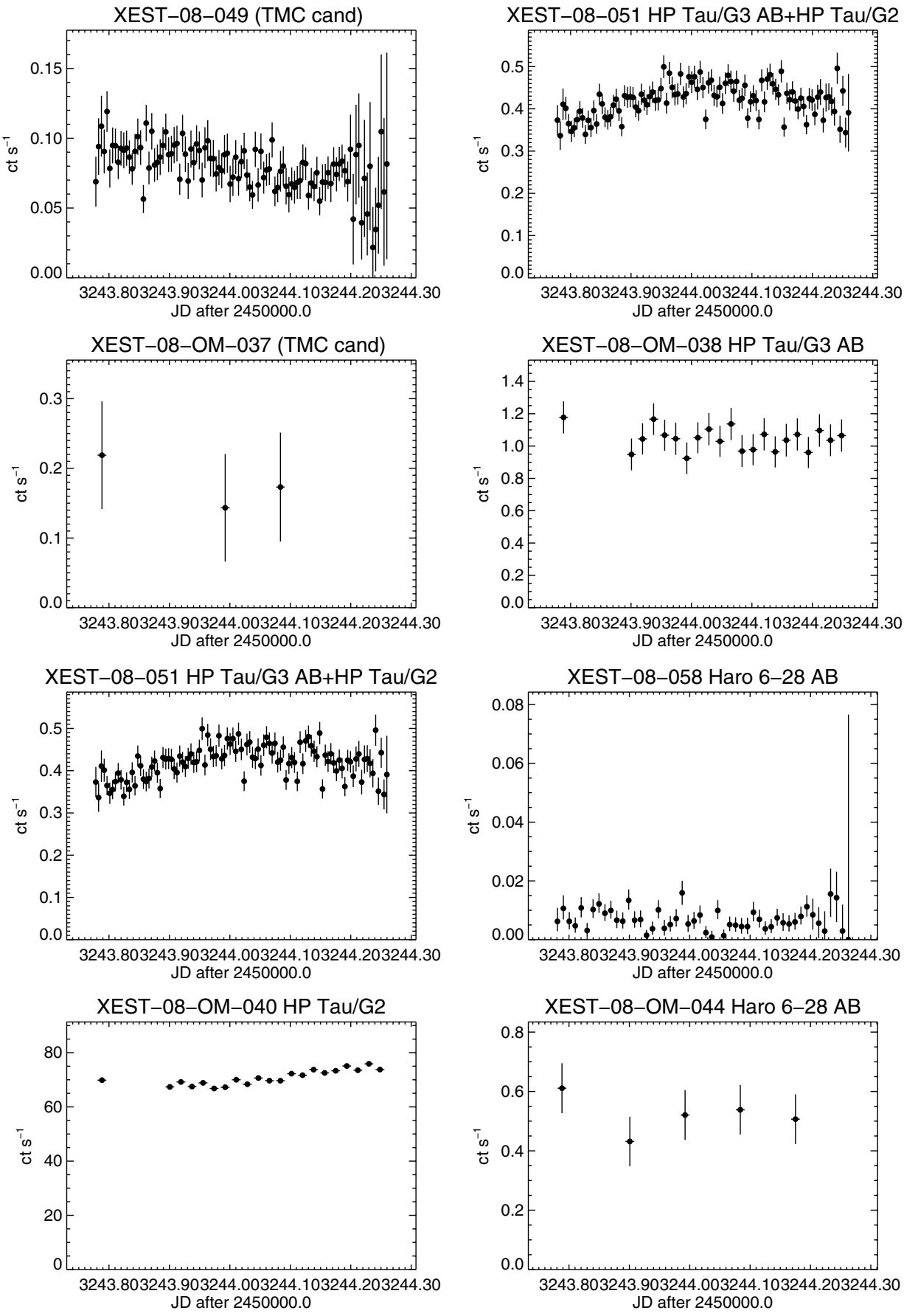

Fig. B.1. continued.

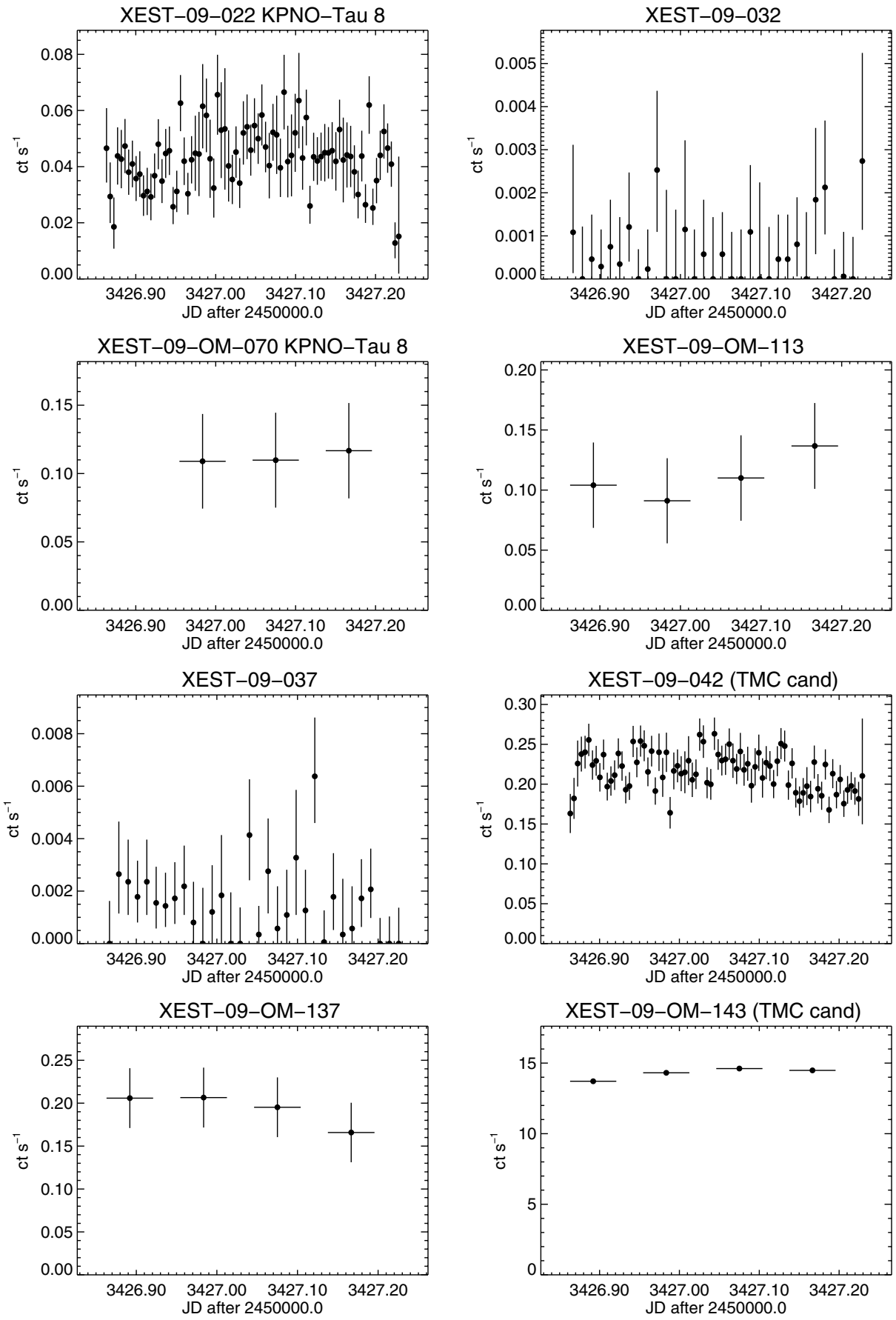

Fig. B.1. continued.

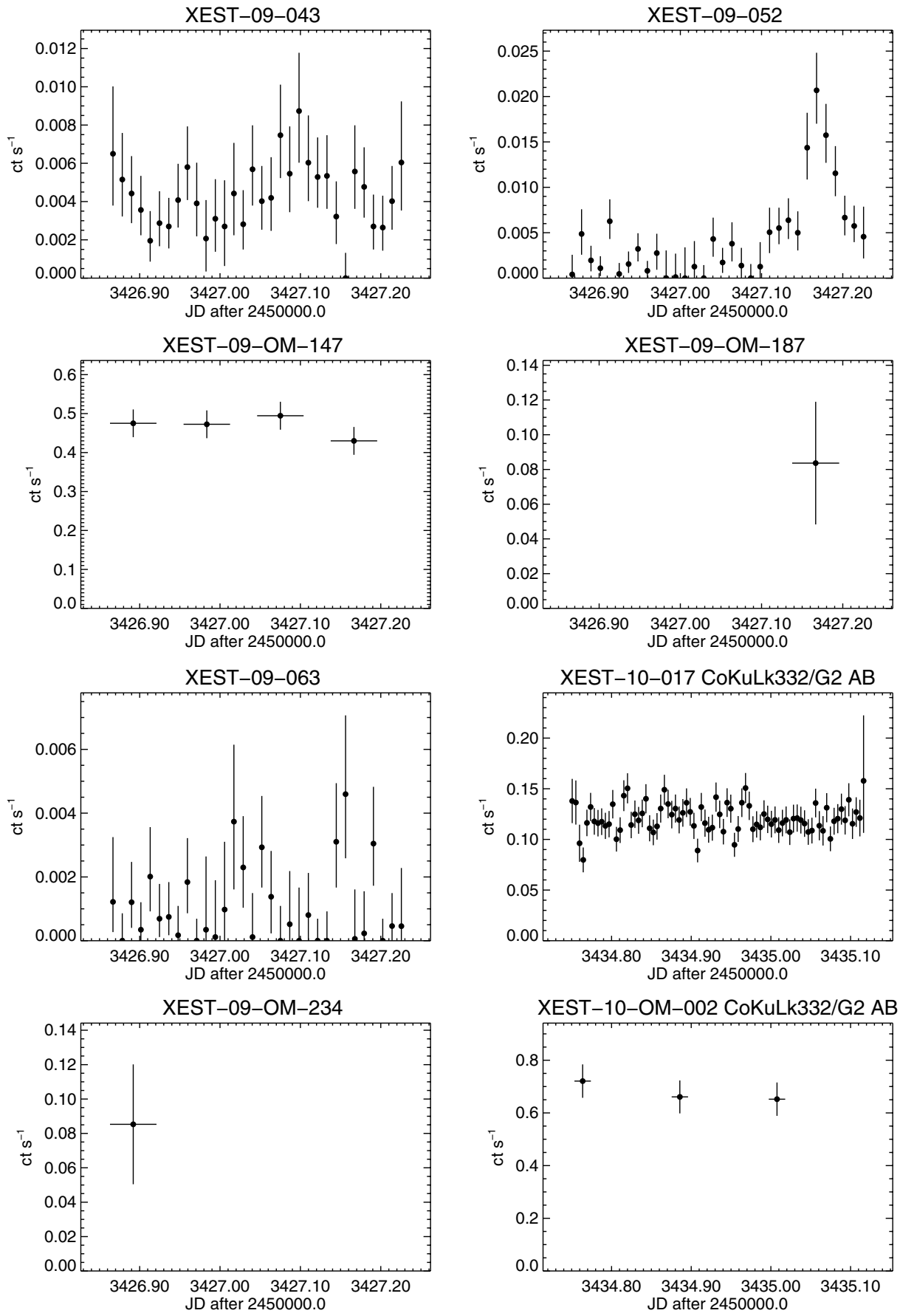

Fig. B.1. continued.

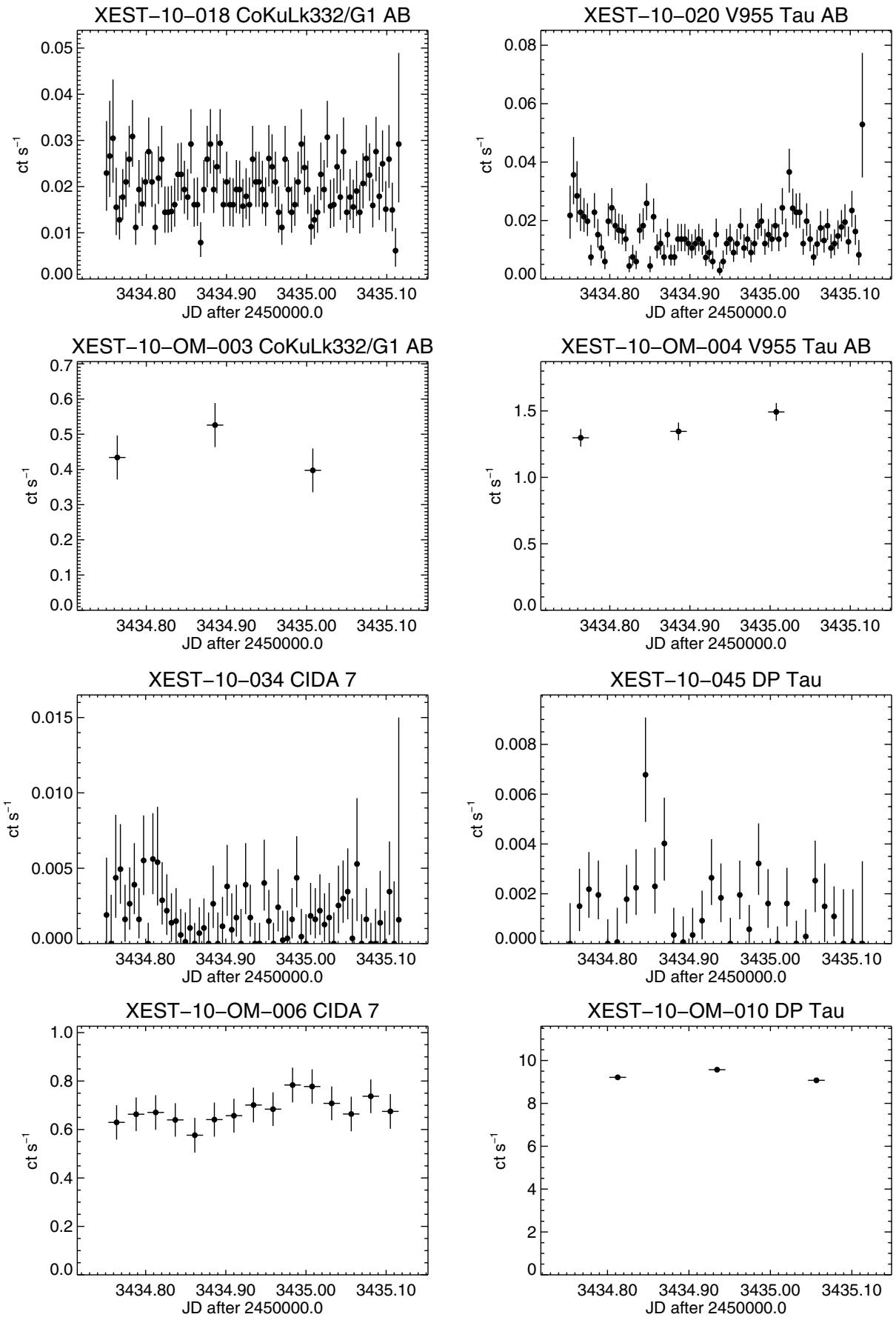

Fig. B.1. continued.

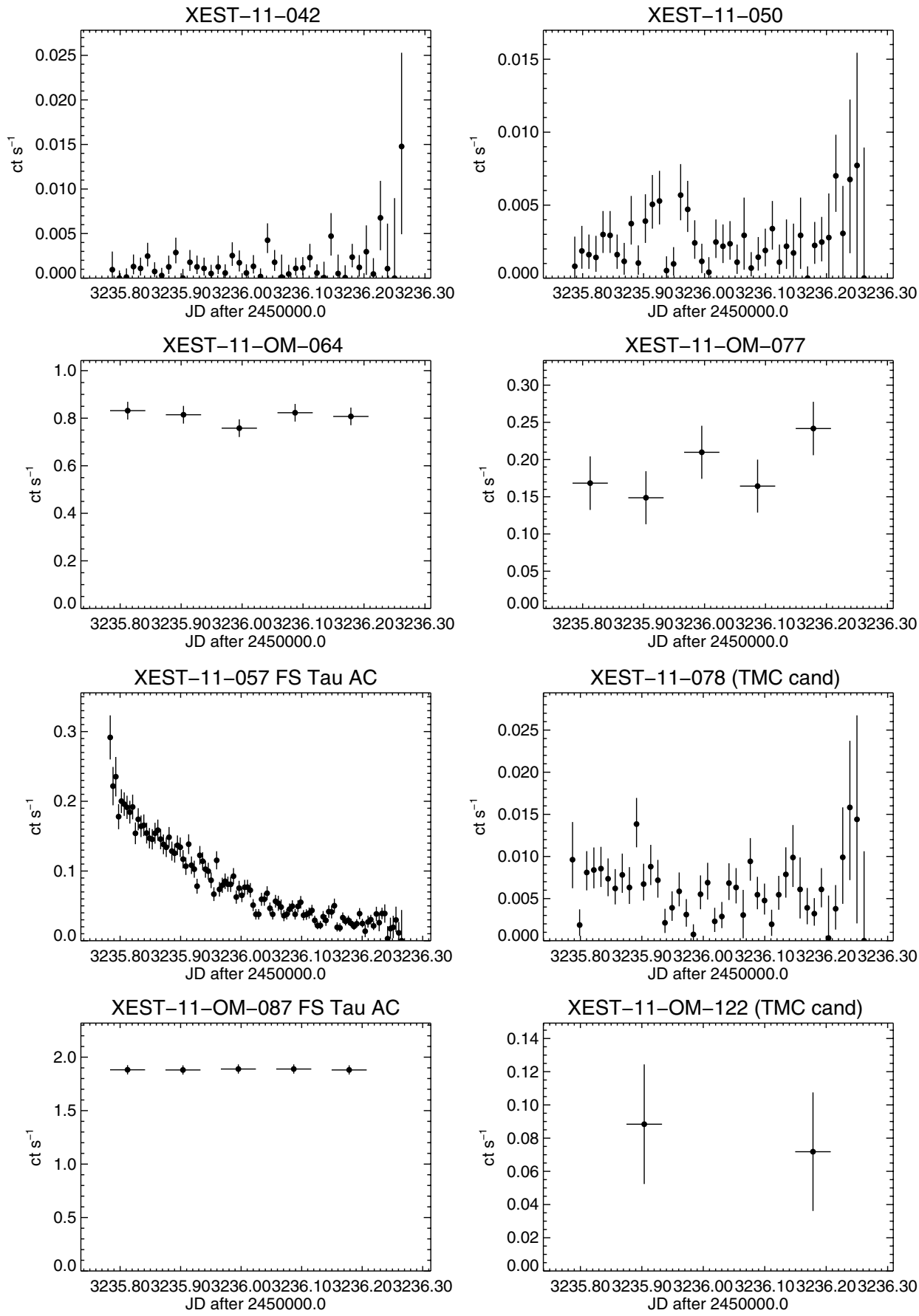

Fig. B.1. continued.

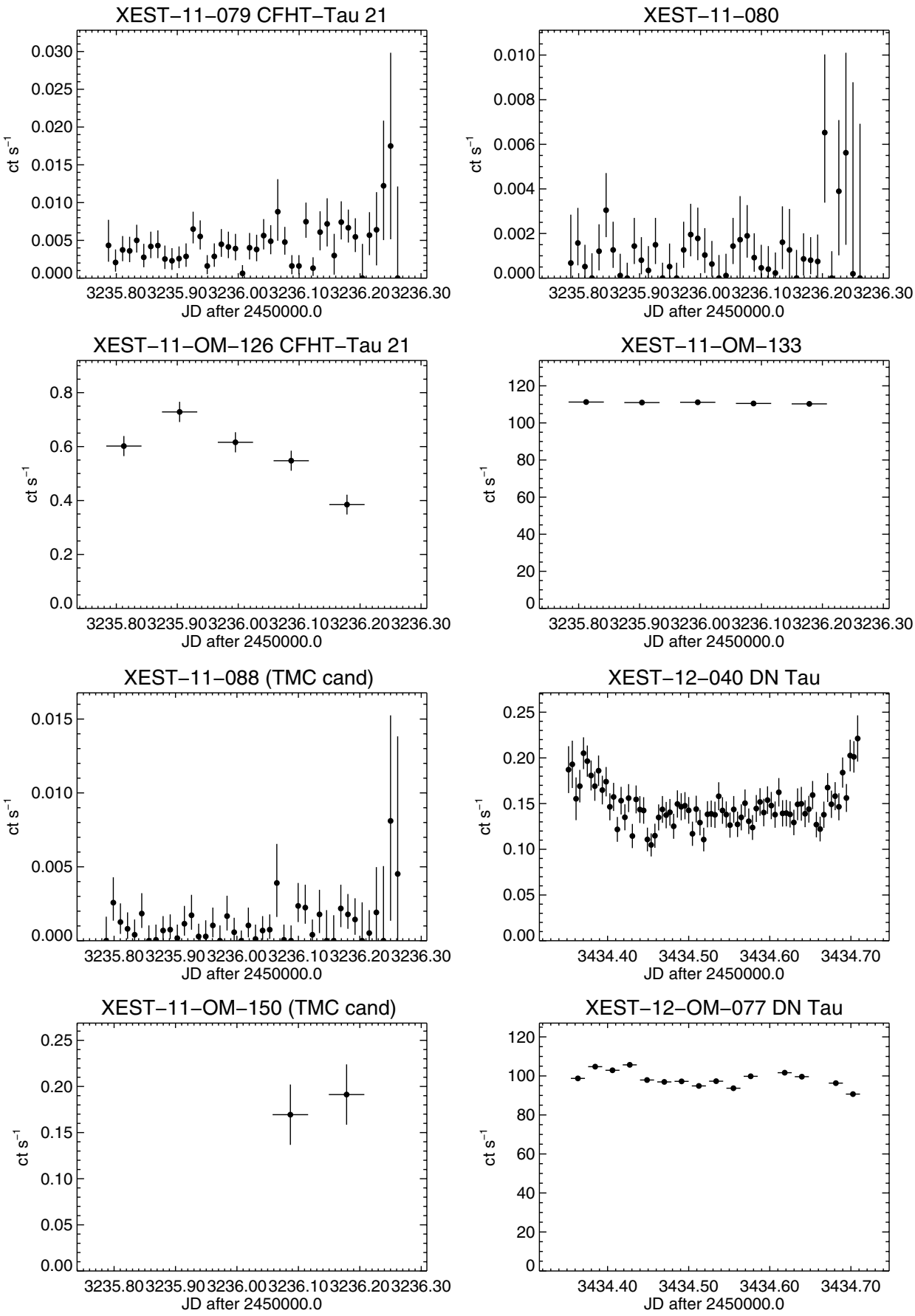

Fig. B.1. continued.

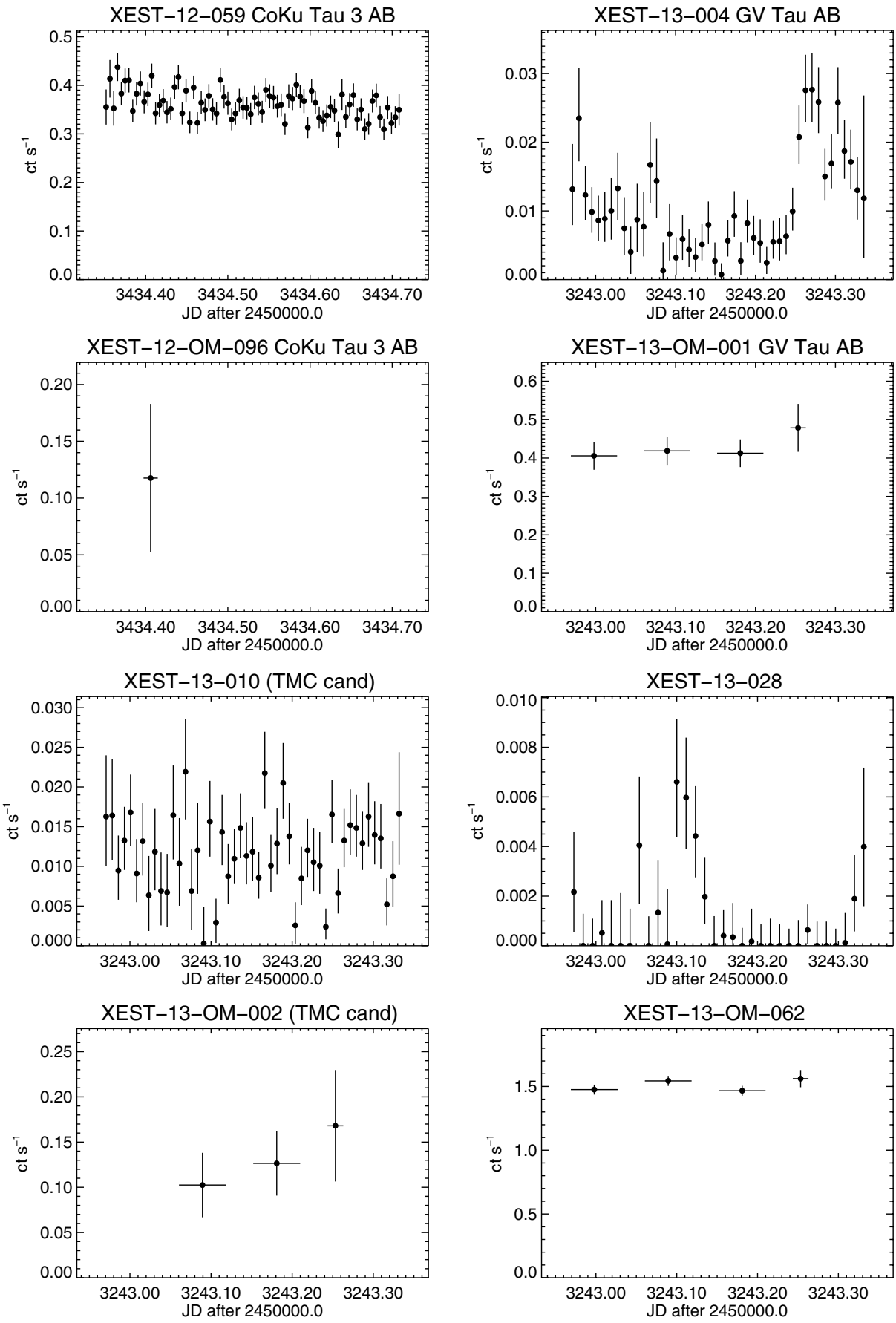

Fig. B.1. continued.

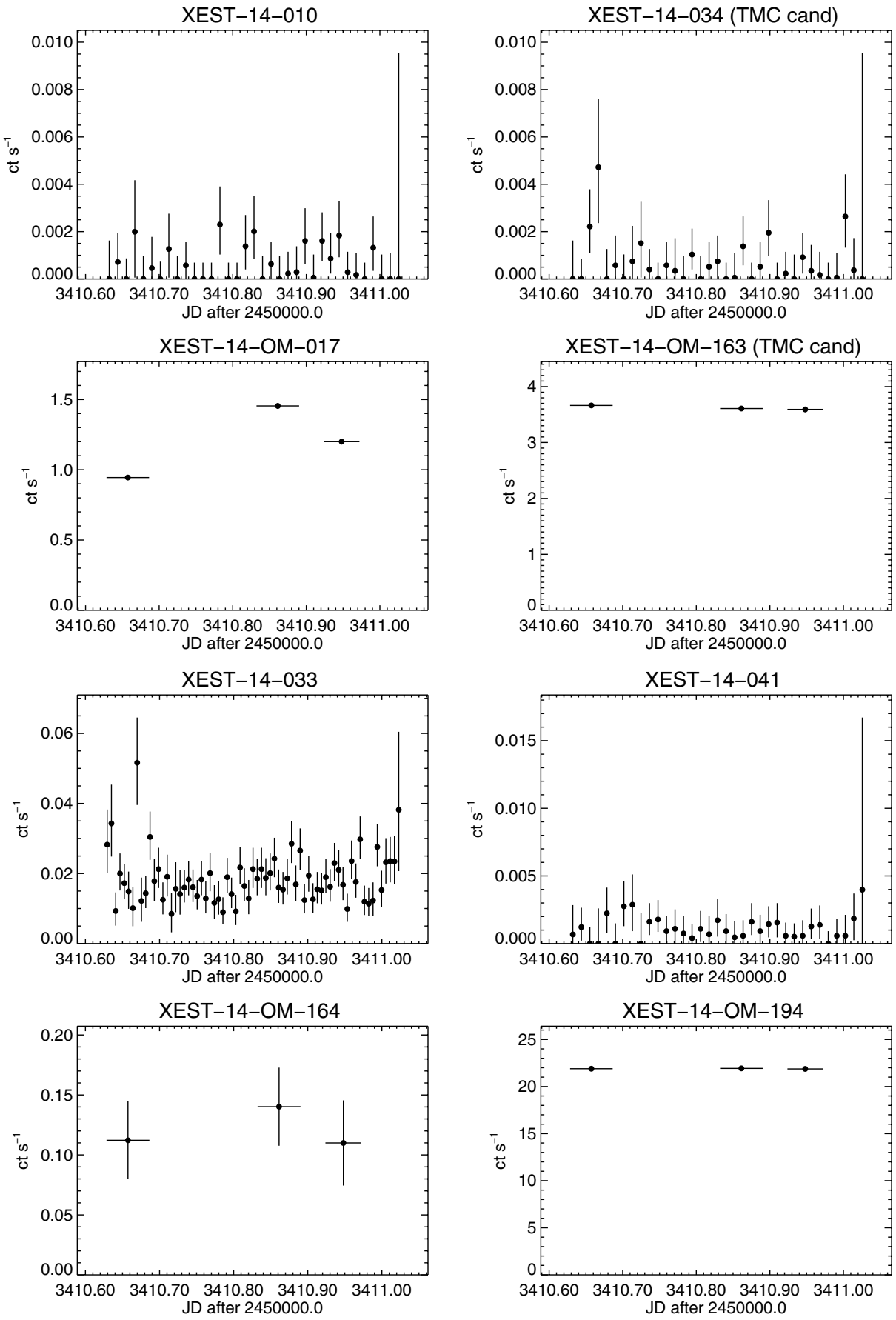

Fig. B.1. continued.

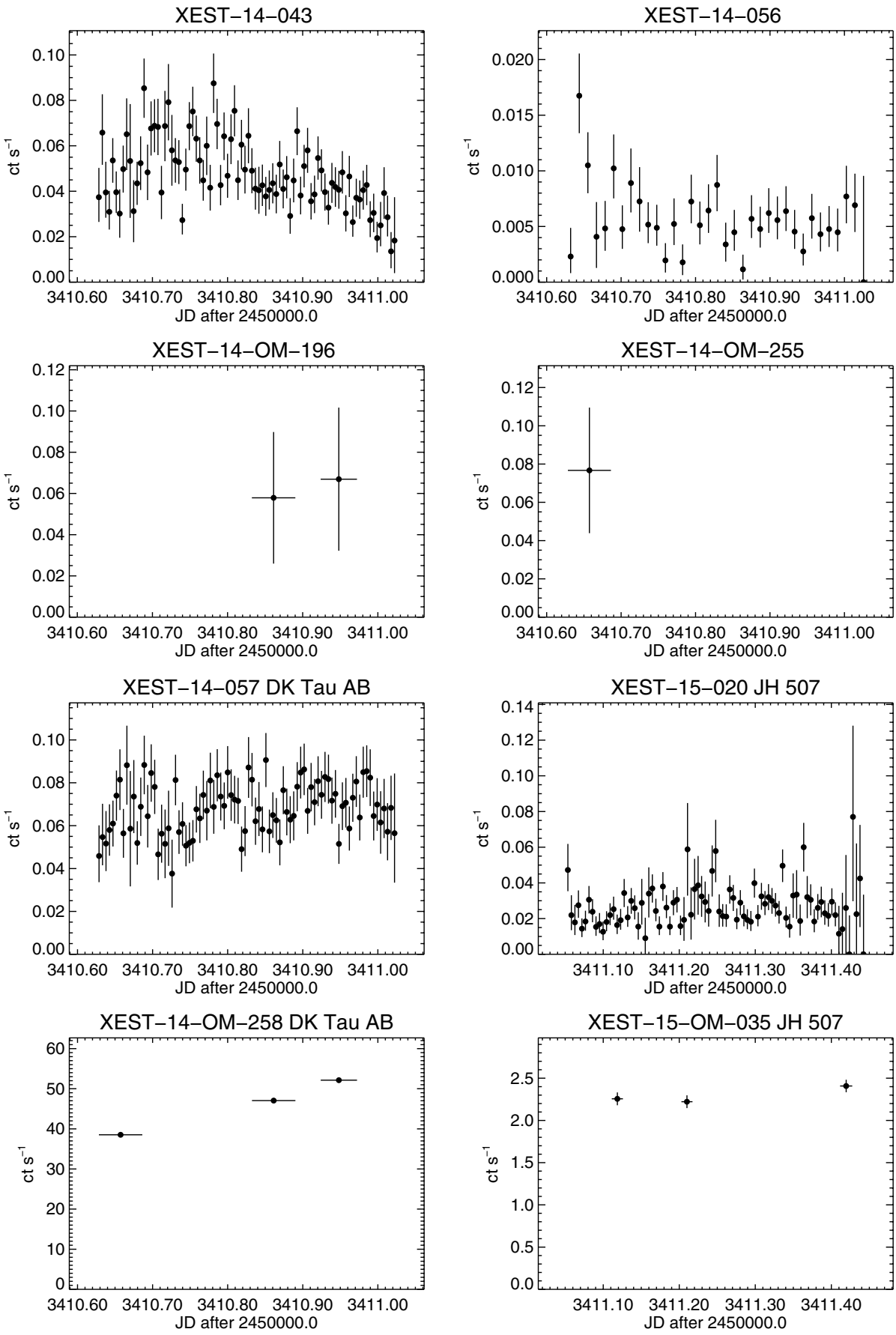

Fig. B.1. continued.

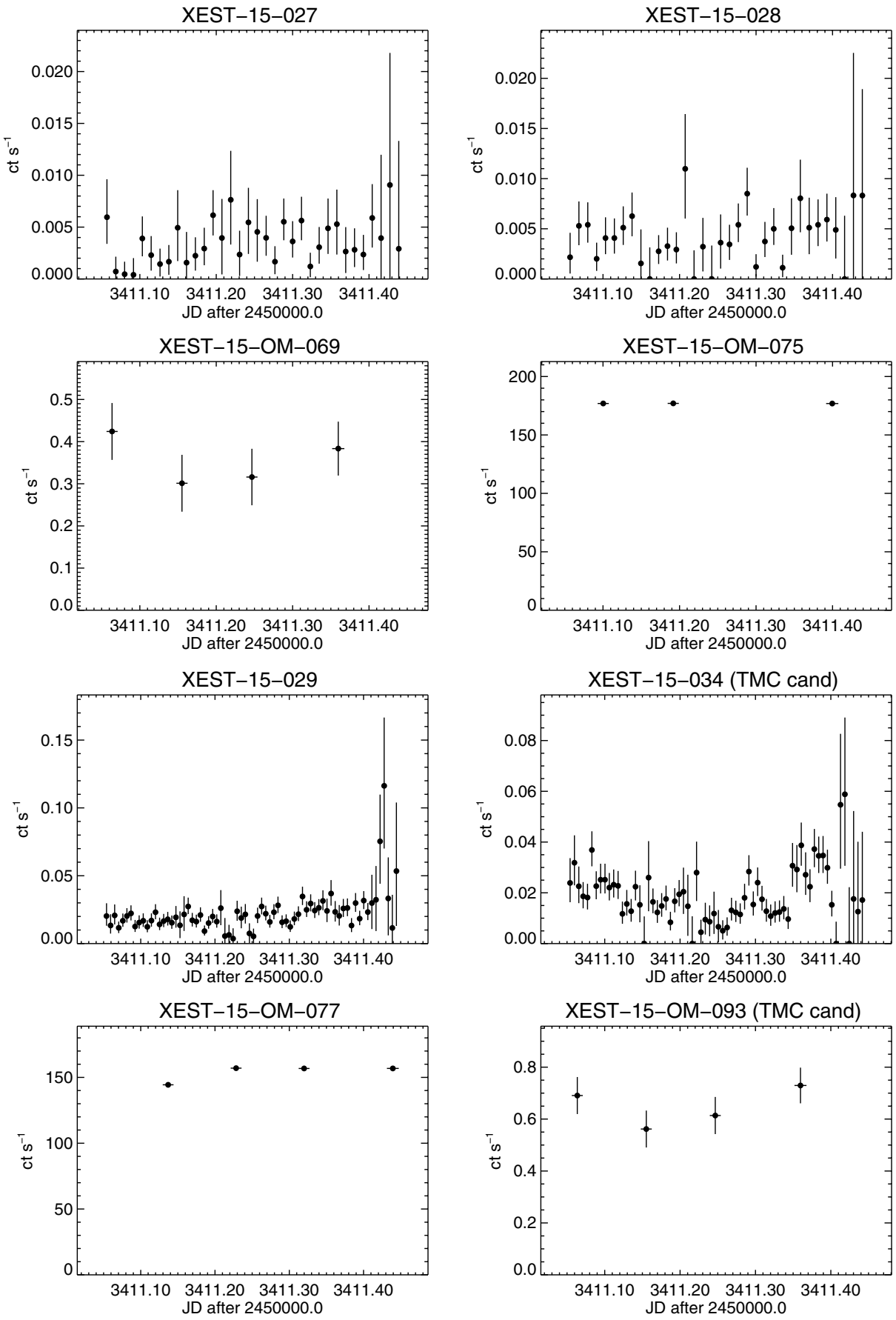

Fig. B.1. continued.

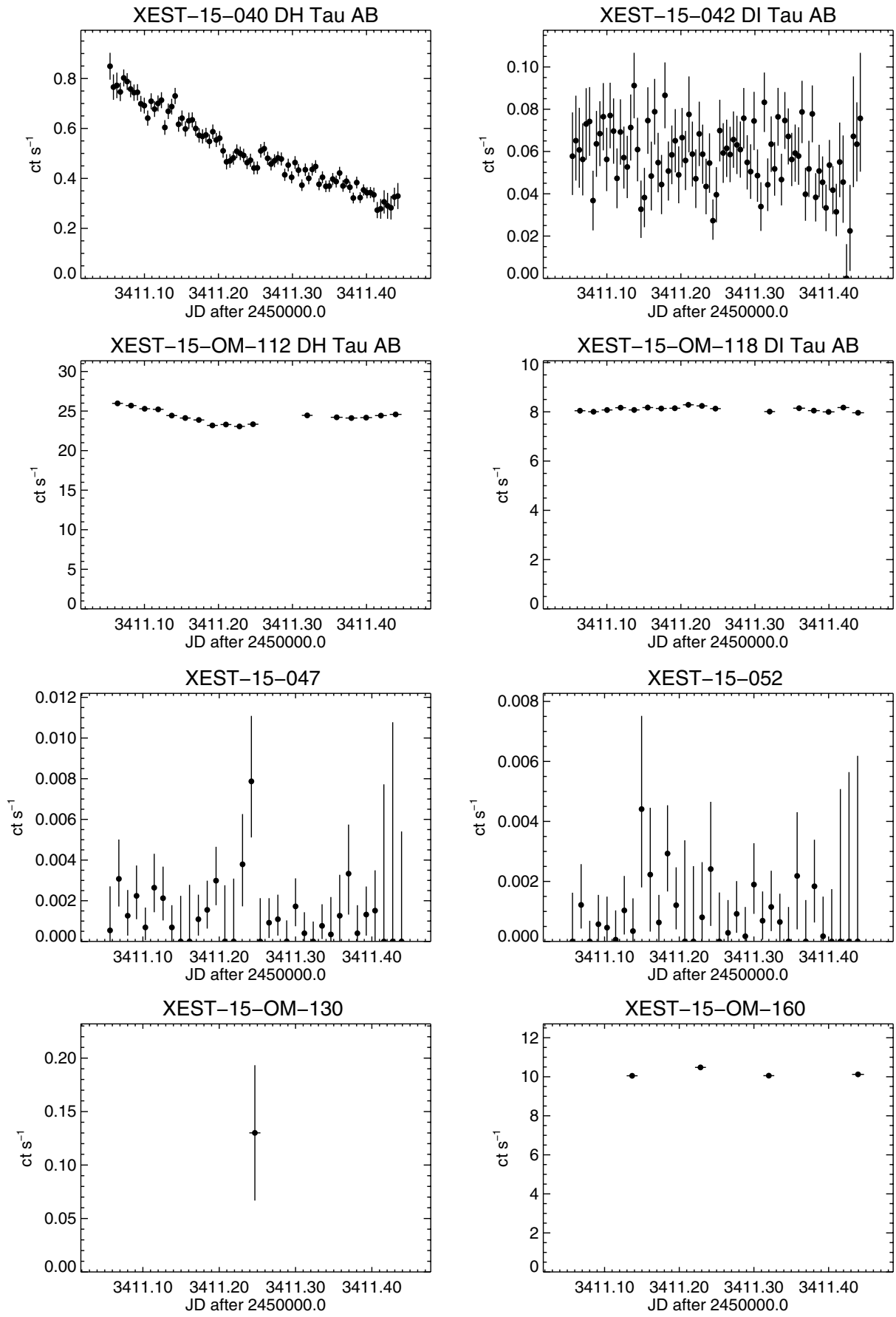

Fig. B.1. continued.

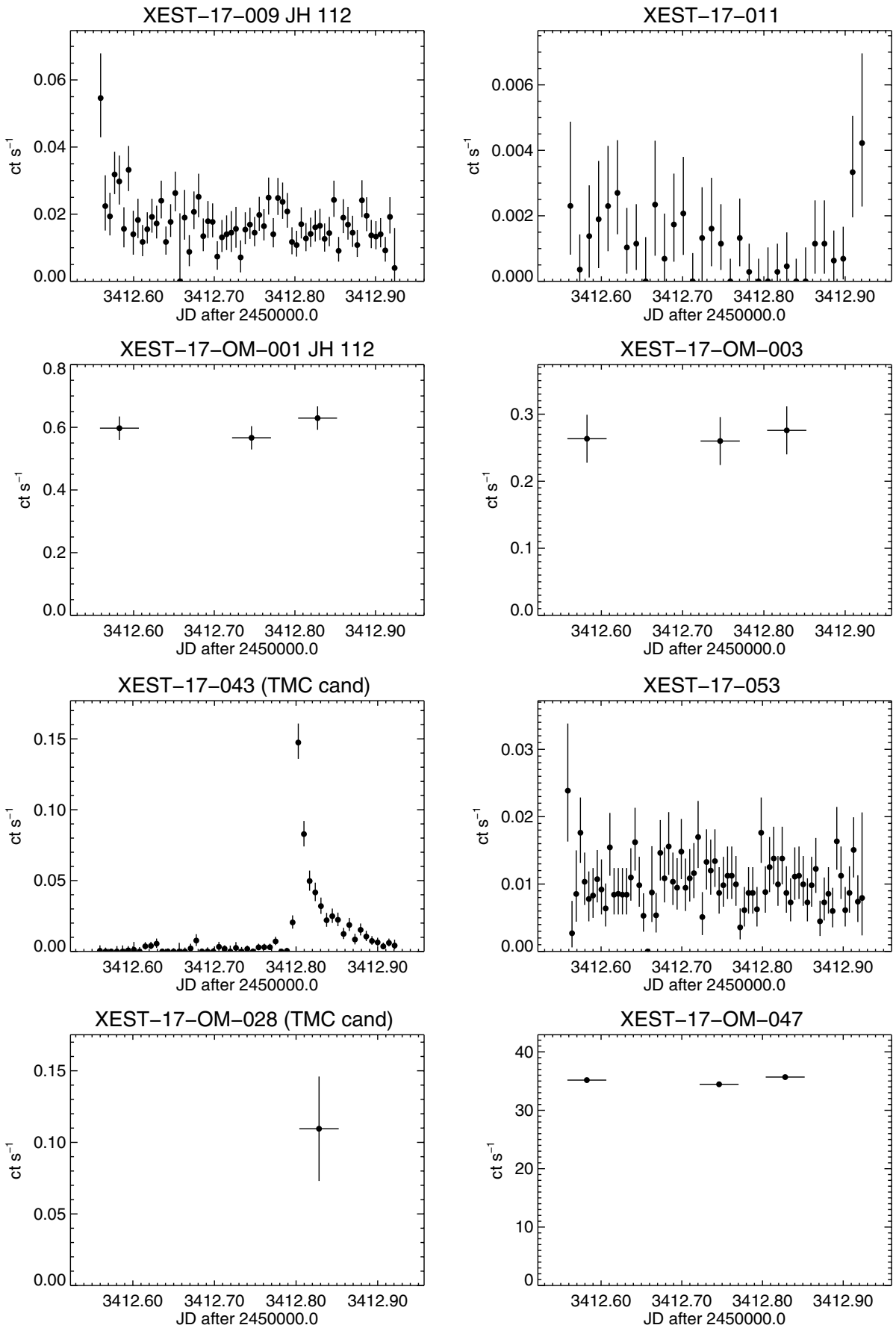

Fig. B.1. continued.

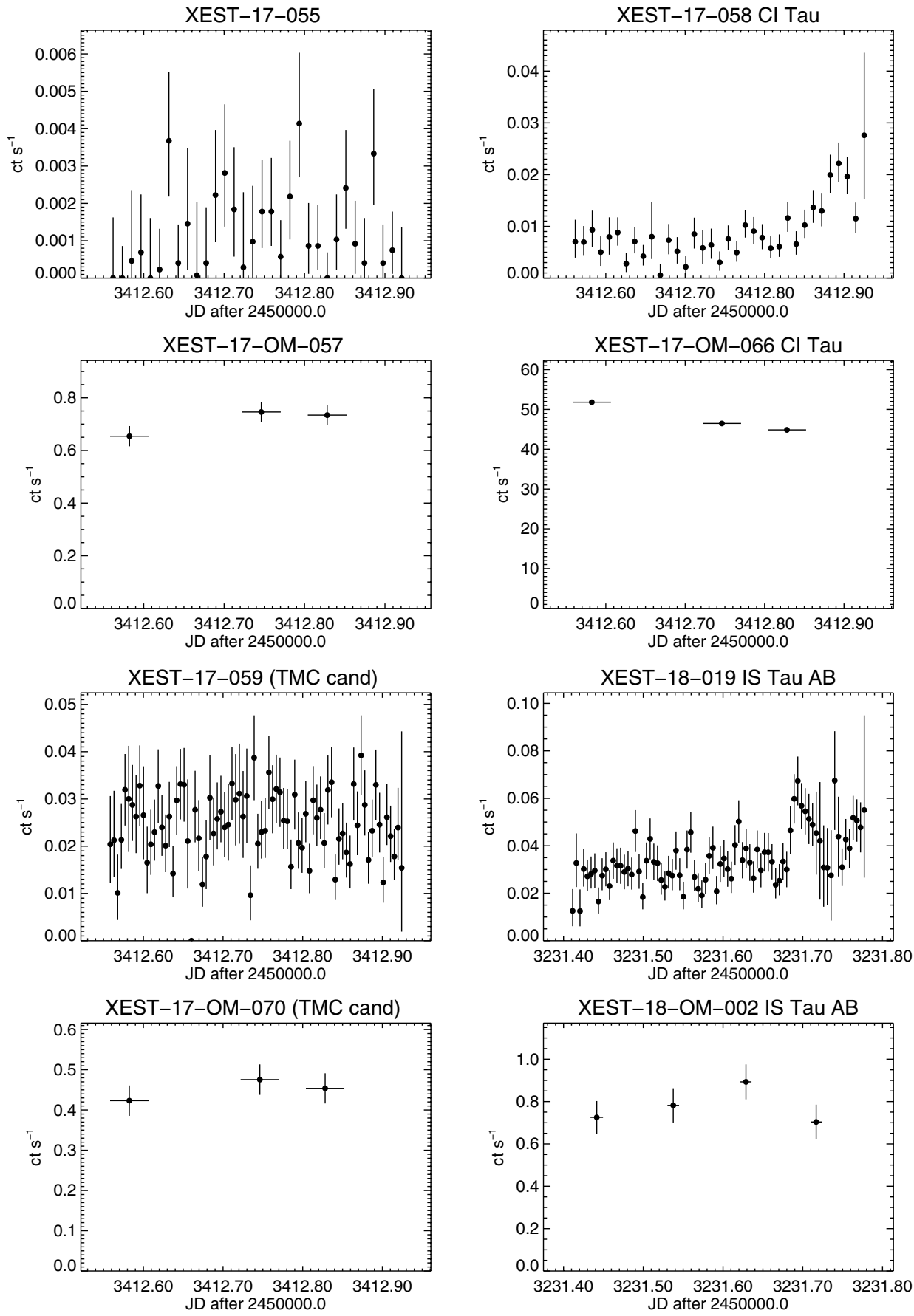

Fig. B.1. continued.

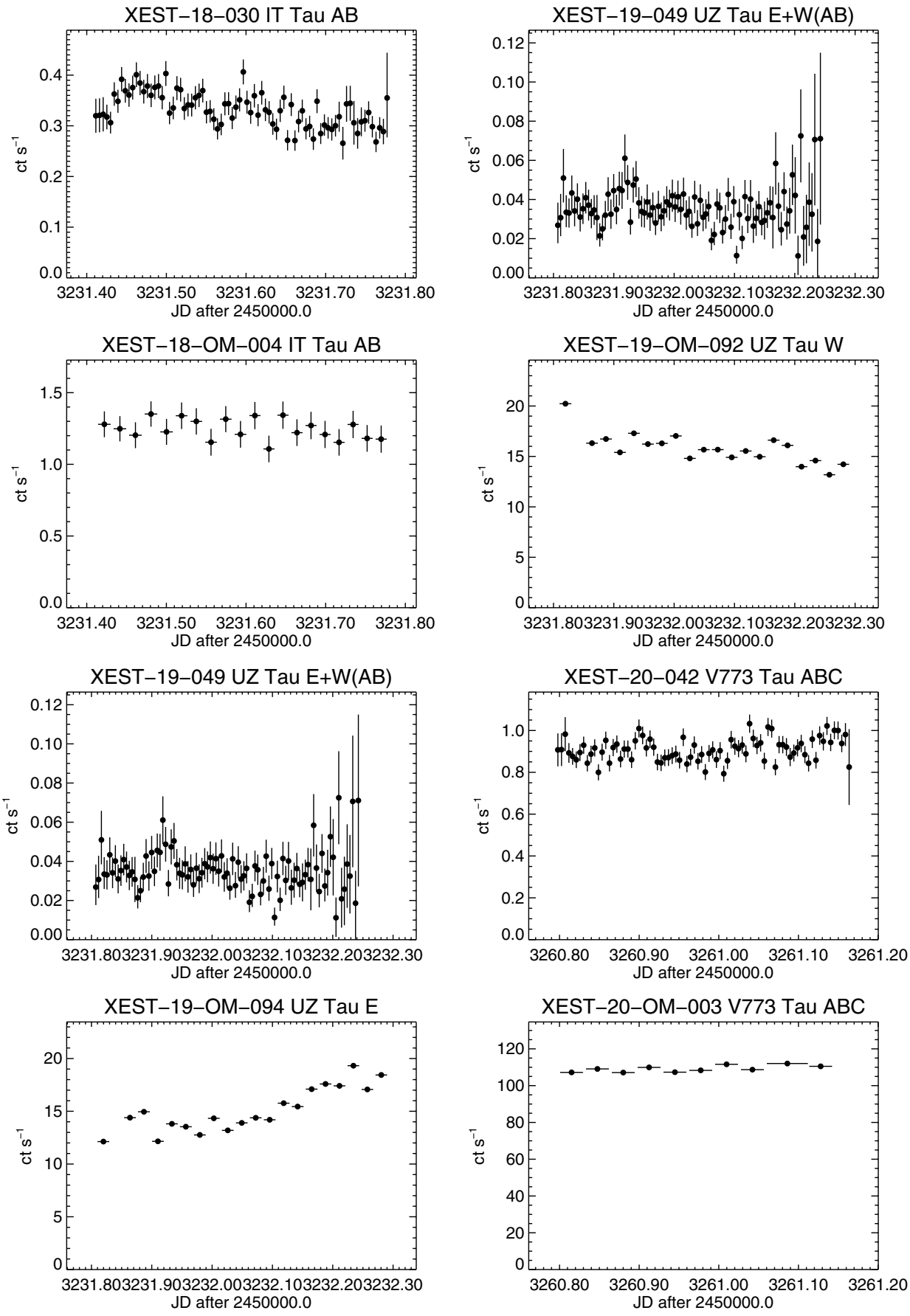

Fig. B.1. continued.

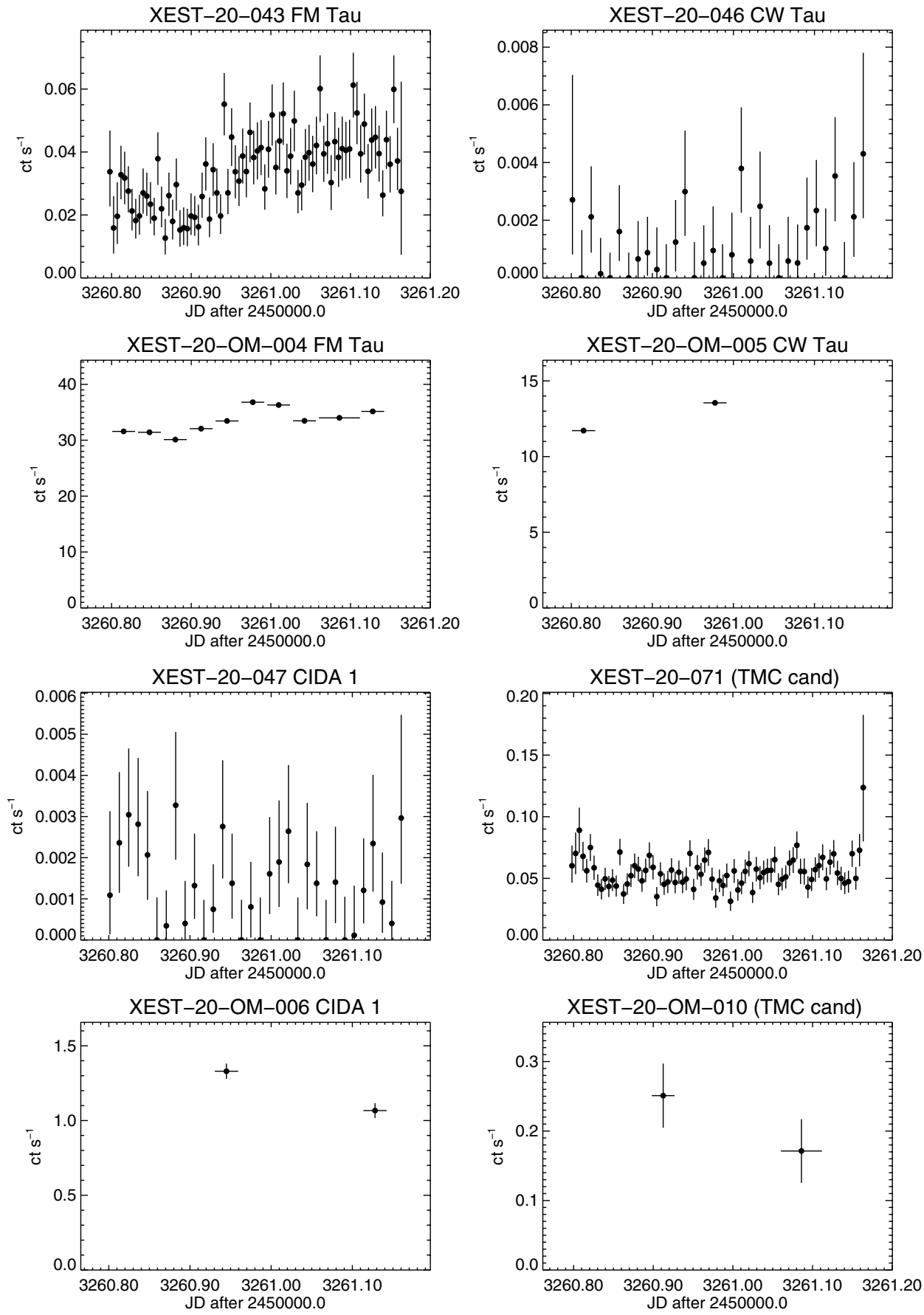

Fig. B.1. continued.

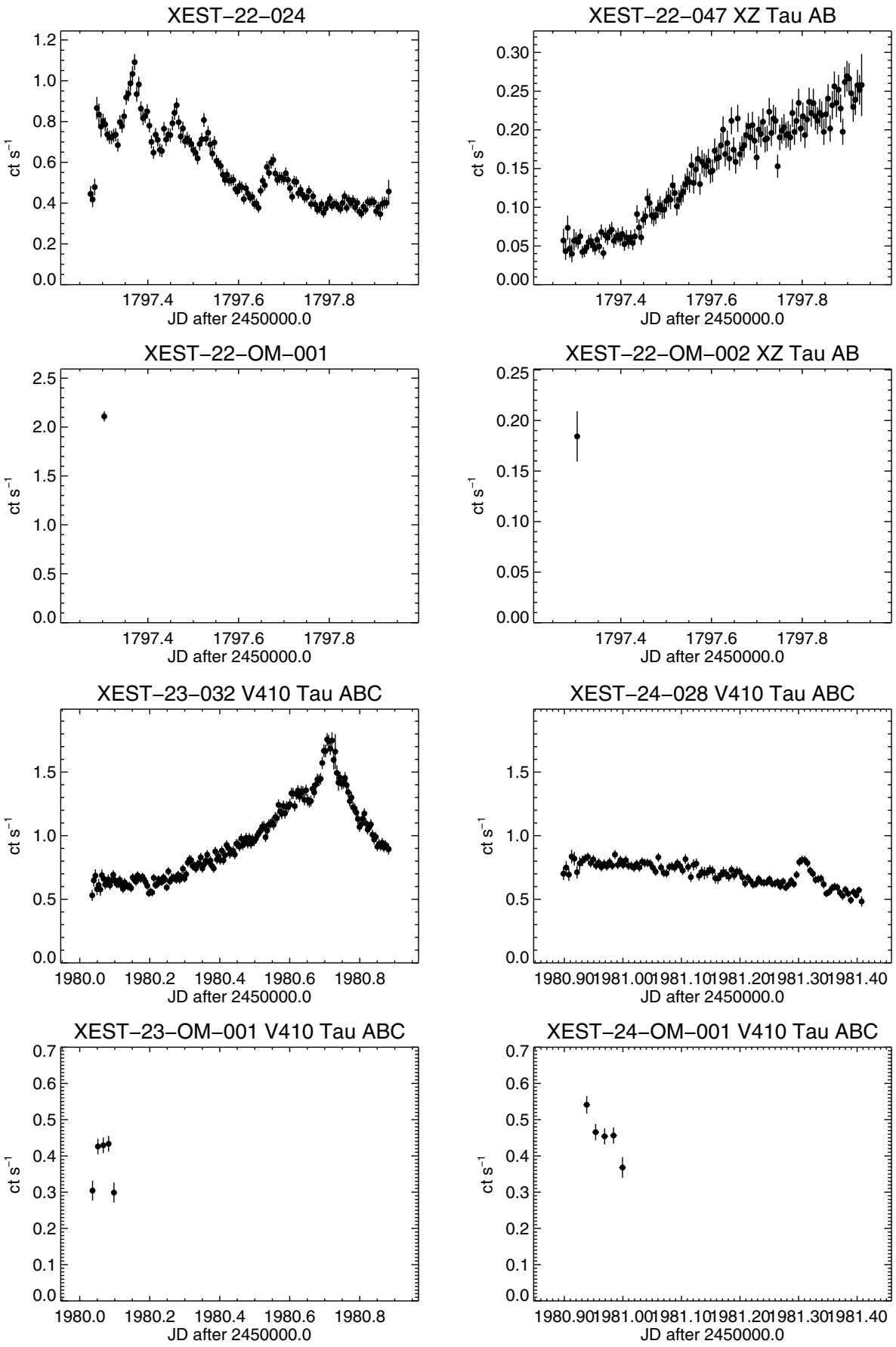

Fig. B.1. continued.

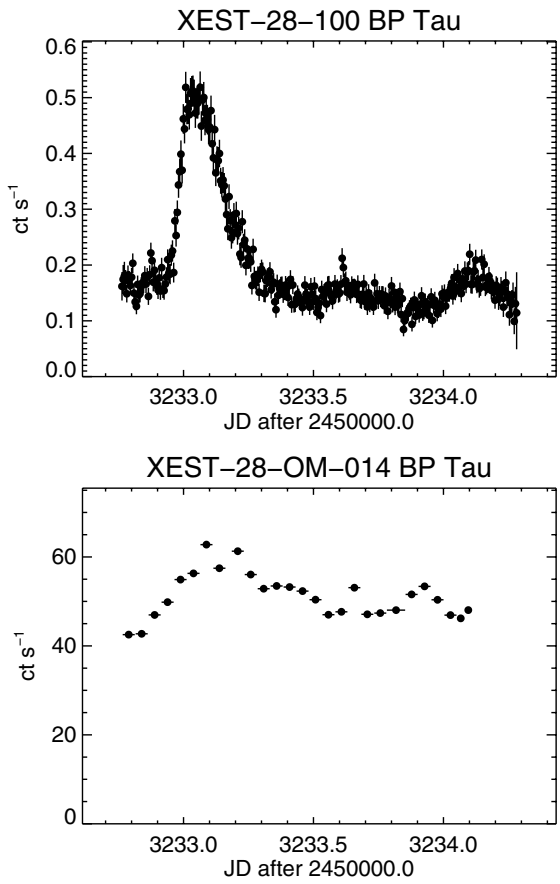

Fig. B.1. continued.